

# Modeling massive multivariate spatial data with the basis graphical lasso

Mitchell Krock<sup>1</sup>, William Kleiber<sup>2</sup>, Dorit Hammerling<sup>3</sup>, and Stephen Becker<sup>2</sup>

February 28, 2025

## Abstract

We propose a new modeling framework for highly multivariate spatial processes that synthesizes ideas from recent multiscale and spectral approaches with graphical models. The basis graphical lasso writes a univariate Gaussian process as a linear combination of basis functions weighted with entries of a Gaussian graphical vector whose graph is estimated from optimizing an  $\ell_1$  penalized likelihood. This paper extends the setting to a multivariate Gaussian process where the basis functions are weighted with Gaussian graphical vectors. We motivate a model where the basis functions represent different levels of resolution and the graphical vectors for each level are assumed to be independent. Using an orthogonal basis grants linear complexity and memory usage in the number of spatial locations, the number of basis functions, and the number of realizations. An additional fusion penalty encourages a parsimonious conditional independence structure in the multilevel graphical model. We illustrate our method on a large climate ensemble from the National Center for Atmospheric Research’s Community Atmosphere Model that involves 40 spatial processes.

KEYWORDS: MULTIVARIATE GAUSSIAN PROCESS, NONSTATIONARY, GRAPHICAL LASSO, SPATIAL BASIS FUNCTION, EMPIRICAL ORTHOGONAL FUNCTION, LARGE ENSEMBLE, CLIMATE MODEL

## 1 Introduction

The past twenty years have seen a surge of interest in developing models for multivariate spatial processes. The major obstacle lies in defining valid cross-covariance functions that can characterize complex interactions between multiple processes; the primary difficulty is

---

<sup>1</sup>Department of Statistics, Rutgers University. Corresponding author e-mail: [mk1867@stat.rutgers.edu](mailto:mk1867@stat.rutgers.edu)

<sup>2</sup>Department of Applied Mathematics, University of Colorado Boulder

<sup>3</sup>Department of Applied Mathematics and Statistics, Colorado School of Mines

that the cross-covariance and marginal covariance functions must work together to provide a nonnegative definite matrix function. Most research has focused on exploring new models or new approaches for defining cross-covariances that are valid for a handful of processes. Many applied problems, such as those in statistical climatology, involve datasets with dozens to hundreds of variables, and most existing approaches fail as strategies to model and understand relevant dependencies between variables.

The main extant approaches to generating valid multivariate spatial models are reviewed by Genton and Kleiber (2015) and include covariance convolution and kernel convolution (Gaspari and Cohn, 1999; Majumdar and Gelfand, 2007; Majumdar et al., 2010; Ver Hoef and Barry, 1998), the linear model of coregionalization (LMC) (Goulard and Voltz, 1992; Schmidt and Gelfand, 2003; Wackernagel, 2003; Gelfand et al., 2004), latent dimensions (Apanasovich and Genton, 2010), dynamical models (Shaddick and Wakefield, 2002; Calder, 2007; Ippoliti et al., 2012) conditional Bayesian hierarchical structures (Le and Zidek, 2006; Pollice and Jona Lasinio, 2010), and direct specification as in the multivariate Matérn (Gneiting et al., 2010; Apanasovich et al., 2012) and nonstationary extensions (Kleiber and Nychka, 2012; Kleiber and Porcu, 2014). All of these models are designed to handle a few variables, typically fewer than five.

Some groups have recently turned attention to the highly-multivariate problem, which often also involves massive numbers of spatial locations. Even with valid covariance and cross-covariance functions specified, likelihood computations for  $p$ -variate Gaussian processes at  $n$  spatial locations scale as  $\mathcal{O}(p^3n^3)$ , which is unacceptable for applications involving high-dimensional processes. One of the first works to tackle highly multivariate processes, Furrer and Genton (2011), introduces “aggregation cokriging,” but this work only addresses prediction and not the modeling nor understanding of highly multivariate spatial data. Several adaptations of the LMC (Guinness, 2018; Taylor-Rodriguez et al., 2019; Bruinsma et al., 2020) are capable of handling large multivariate data, but each still requires constructing a nonstationary covariance model for latent processes. Kleiber et al. (2019) introduce an approach that generalizes LatticeKrig (Nychka et al., 2015) to the multivariate case and can handle massive spatial data, relying on compactly supported basis functions and spatial autoregressive Gaussian Markov random field models for stochastic coefficients. Dey et al.

(2020) recently introduced an idea utilizing Gaussian graphical models that can approximate the multivariate Matérn, but, like the LMC, it does not directly address the issue of nonstationarity in the covariance and cross-covariance functions. Our approach also relies on Gaussian graphical models but avoids directly modeling the covariance and cross-covariance functions by using a basis decomposition. In addition to nonstationarity granted by judicious choice of basis functions and stochastic coefficient structure, employing *orthogonal* basis functions allows for rapid computation with non-gridded high-dimensional multivariate spatial data.

To introduce the basic ideas, let us fix some notation. The  $p$ -variate observational Gaussian process model under consideration is

$$\begin{pmatrix} Y_1(\mathbf{s}) \\ \vdots \\ Y_p(\mathbf{s}) \end{pmatrix} = \begin{pmatrix} \mu_1(\mathbf{s}) \\ \vdots \\ \mu_p(\mathbf{s}) \end{pmatrix} + \begin{pmatrix} Z_1(\mathbf{s}) \\ \vdots \\ Z_p(\mathbf{s}) \end{pmatrix} + \begin{pmatrix} \varepsilon_1(\mathbf{s}) \\ \vdots \\ \varepsilon_p(\mathbf{s}) \end{pmatrix} \quad (1)$$

or in vector form,  $\mathbf{Y}(\mathbf{s}) = \boldsymbol{\mu}(\mathbf{s}) + \mathbf{Z}(\mathbf{s}) + \boldsymbol{\varepsilon}(\mathbf{s})$ . Here,  $\mathbf{Y}(\mathbf{s}) = (Y_1(\mathbf{s}), \dots, Y_p(\mathbf{s}))^T$  is the observed process at location  $\mathbf{s} \in \mathbb{R}^d$  with mean  $\boldsymbol{\mu}(\mathbf{s}) = (\mu_1(\mathbf{s}), \dots, \mu_p(\mathbf{s}))^T$  and spatially correlated stochastic variation  $\mathbf{Z}(\mathbf{s}) = (Z_1(\mathbf{s}), \dots, Z_p(\mathbf{s}))^T$ , which we assume to be a multivariate Gaussian process. The observations are subject to noise  $\boldsymbol{\varepsilon}(\mathbf{s}) = (\varepsilon_1(\mathbf{s}), \dots, \varepsilon_p(\mathbf{s}))^T$ , a mean zero multivariate white noise process with covariance matrix  $\text{Cov}(\boldsymbol{\varepsilon}(\mathbf{s}), \boldsymbol{\varepsilon}(\mathbf{s})) = \text{diag}(\tau_1^2, \dots, \tau_p^2)$ .

A key difficulty in working with multivariate processes is in specifying the matrix-valued covariance,  $\mathbf{C}(\mathbf{s}_1, \mathbf{s}_2) = (C_{ij}(\mathbf{s}_1, \mathbf{s}_2))_{i,j=1}^p$ , where  $C_{ij}(\mathbf{s}_1, \mathbf{s}_2) = \text{Cov}(Z_i(\mathbf{s}_1), Z_j(\mathbf{s}_2))$  are the direct and cross-covariance functions. This matrix function must be carefully constrained in order to be a nonnegative definite matrix function. In particular, for arbitrary locations  $\{\mathbf{s}_i\}_{i=1}^n$ , the block matrix  $\boldsymbol{\Sigma}$  with  $(i, j)$ th block  $\mathbf{C}(\mathbf{s}_i, \mathbf{s}_j)$  must be nonnegative definite. Genton and Kleiber (2015) give an overview of cross-covariance functions for multivariate geostatistics which is still relatively up-to-date.

We introduce a model for highly multivariate and nonstationary spatial data that also accommodates estimation and simulation strategies for large networks of observation locations. The essential ideas rely on representing the vector-valued process in a basis expansion with sparsity-inducing Gaussian graphical modeling of the stochastic coefficients. We propose a penalized likelihood framework for estimation and associated optimization algorithms. The

method is illustrated on a challenging climate data science problem involving  $p = 40$  spatial processes from an atmospheric model at thousands of locations that exhibit strong nonstationarities and cross-process dependencies. Our model provides straightforward interpretations of cross-process dependences, which for the climate data example identify scientifically meaningful and justifiable relationships.

## 2 Methodology

Our approach relies on a basis expansion of the spatially-correlated components of  $\mathbf{Z}(\mathbf{s})$ :

$$Z_i(s) = \sum_{\ell=1}^L W_{i\ell} \phi_{\ell}(s) \quad (i = 1, \dots, p) \quad (2)$$

for some classes of basis functions  $\{\phi_{\ell}\}$  and stochastic coefficients  $\{W_{i\ell}\}$ . For fixed  $i$ , this representation subsumes many popular approaches in the spatial statistical literature that have been primarily explored in the univariate setting, including discretized spectral methods, low rank approaches, and empirical orthogonal functions among others, despite potential limitations depending upon the choice of basis function (Stein, 2014). Few extensions to the multivariate case (2) have been made, with Kleiber et al. (2019) being a notable case. In Section 2.1, we show how the univariate basis graphical lasso directly extends to the multivariate setting (2), and in Section 2.2, we discuss an alternative which is more appropriate for massive multivariate spatial data.

### 2.1 Basis Graphical Lasso

Our modeling and optimization strategy follows from extensions to our prior work, which we discuss and connect to the multivariate problem in this section. In Krock et al. (2020), we introduced the basis graphical lasso (BGL) to model (2) for the univariate case  $p = 1$ . The goal of the BGL is to obtain a sparse nonparametric estimate for the precision matrix  $Q$  of the mean zero Gaussian graphical vector  $\mathbf{W} = (W_1, \dots, W_L)^T$  when  $Z(\mathbf{s}) = \sum_{\ell=1}^L W_{\ell} \phi_{\ell}(\mathbf{s})$ . In other words, we build a Gaussian process by fitting a Gaussian graphical model to the random coefficients of fixed basis functions. Recall that the sparsity pattern of the precision matrix encodes conditional independencies between random variables, with  $Q_{ij} = 0$  if and only if



$W_i$  and  $W_j$  are conditionally independent given all other entries of  $\mathbf{W}$ . This information is commonly visualized with an undirected graph known as a Gaussian graphical model, where vertices symbolize variables and the lack of an edge between two vertices indicates such a conditional independence (Rue and Held, 2005). Inspired by the graphical lasso (Friedman et al., 2008), we use an  $\ell_1$  penalized likelihood to estimate the graphical model, but in the standard graphical lasso setting  $\mathbf{W}$  is observed directly, whereas our model includes basis functions and noise. Our BGL method is viable for a very large sample size ( $n$ ), and multiple realizations ( $m$ ) are preferred but not required. Note that this formulation is opposite to the LMC, which is not typically used in a univariate setting but estimates the deterministic weights of individual Gaussian processes. We claim that the BGL generalizes to the multivariate setting and also that the optimization routine enjoys a similar computational framework.

With  $\mathbf{W}_\ell = (W_{1\ell}, \dots, W_{p\ell})^T \sim N(\mathbf{0}, \mathbf{Q}_\ell^{-1})$ , the multivariate basis model (2) alternatively can be written

$$\mathbf{Z}(\mathbf{s}) = \sum_{\ell=1}^L \phi_\ell(\mathbf{s}) \mathbf{W}_\ell \quad (3)$$

so that each basis function is weighted with a  $p$ -variate random vector. Assuming the weight vectors are independent means that this model amounts to characterizing the inverse covariance matrices  $\{\mathbf{Q}_1, \dots, \mathbf{Q}_L\}$ . In contrast, the LMC considers (3) where  $\{\phi_1(\mathbf{s}), \dots, \phi_L(\mathbf{s})\}$  are independent Gaussian processes with deterministic weights. We note that recent variants of the LMC (Taylor-Rodriguez et al., 2019; Bruinsma et al., 2020) can handle a large number of variables, and in fact orthogonal basis functions are also exploited for computational gains in the latter work, but such techniques ultimately amount to efficiently modeling spatially-dense univariate Gaussian processes (e.g., Datta et al. (2016); Titsias (2009)). The semiparametric latent factor model (Teh et al., 2005) shares a setup similar to the LMC where a multi-output Gaussian process is represented as a linear mixture of independent univariate Gaussian processes. With these models, weight vectors of the independent univariate Gaussian processes and (stationary) covariance parameters must be estimated. On the other hand, our approach associates each basis function with a  $p$ -variate Gaussian graphical model, which is much faster from a computational point of view and automatically produces nonstationary covariance and cross-covariance functions with straightforward interpretations.

Let us assume  $\boldsymbol{\mu} \equiv 0$  in (1) for simplicity of exposition. In a typical mean function regression context, we can use generalized least squares and profiled likelihoods to estimate the regression coefficients. Given data at locations  $\mathbf{s}_1, \dots, \mathbf{s}_n$ , form the observation vector  $\mathbf{Y} = (\mathbf{Y}(\mathbf{s}_1)^T, \dots, \mathbf{Y}(\mathbf{s}_n)^T)^T$ . Suppose we have multiple independent realizations  $\mathbf{Y}_1, \dots, \mathbf{Y}_m$  of  $\mathbf{Y}$ . Up to multiplicative and additive constants not depending on the  $np \times np$  variance-covariance matrix  $\boldsymbol{\Sigma} = \text{Var}(\mathbf{Y})$ , the negative log-likelihood is

$$\log \det \boldsymbol{\Sigma} + \frac{1}{m} \sum_{i=1}^m \mathbf{Y}_i^T \boldsymbol{\Sigma}^{-1} \mathbf{Y}_i. \quad (4)$$

Define the sample covariance  $\mathbf{S} = \frac{1}{m} \sum_{i=1}^m \mathbf{Y}_i \mathbf{Y}_i^T$ . Using the cyclic property of trace, we rewrite the negative log-likelihood as

$$\log \det \boldsymbol{\Sigma} + \text{tr}(\mathbf{S} \boldsymbol{\Sigma}^{-1}) \quad (5)$$

to align with more prevalent notation in graphical lasso literature. Note that  $\mathbf{Y}$  is simply a linear combination of the random coefficient vector  $\mathbf{W} = (\mathbf{W}_1^T, \dots, \mathbf{W}_L^T)^T$  and basis functions, plus noise. That is,  $\mathbf{Y} = \boldsymbol{\Phi} \mathbf{W} + \boldsymbol{\varepsilon}$  for a basis matrix  $\boldsymbol{\Phi}$ , so  $\boldsymbol{\Sigma} = \boldsymbol{\Phi} \mathbf{Q}^{-1} \boldsymbol{\Phi}^T + \mathbf{D}$ . These matrices are defined explicitly in Section 3, but it is important to realize here that the matrix algebra produces the same optimization problem as in the univariate case.

The original BGL solves the  $\ell_1$ -penalized maximum likelihood equation

$$\hat{\mathbf{Q}} \in \arg \min_{\mathbf{Q} \succeq 0} \log \det(\boldsymbol{\Phi} \mathbf{Q}^{-1} \boldsymbol{\Phi}^T + \mathbf{D}) + \text{tr}(\mathbf{S}(\boldsymbol{\Phi} \mathbf{Q}^{-1} \boldsymbol{\Phi}^T + \mathbf{D})^{-1}) + \|\Lambda \circ \mathbf{Q}\|_1. \quad (6)$$

We use the notation  $\mathbf{Q} \succeq 0$  to indicate that  $\mathbf{Q}$  is positive semidefinite. Here,  $\|\Lambda \circ \mathbf{Q}\|_1 = \sum_{i,j} \Lambda_{ij} |\mathbf{Q}_{ij}|$  where  $\Lambda_{ij}$  are nonnegative penalty parameters that encourage sparsity in the estimate. Evaluating (6) requires an expensive  $\mathcal{O}(p^3 n^3)$  Cholesky decomposition. After applying the matrix determinant lemma, the Sherman-Morrison-Woodbury formula, and the cyclic property of trace, we can equivalently minimize

$$\log \det (\mathbf{Q} + \boldsymbol{\Phi}^T \mathbf{D}^{-1} \boldsymbol{\Phi}) - \log \det \mathbf{Q} - \text{tr} (\boldsymbol{\Phi}^T \mathbf{D}^{-1} \mathbf{S} \mathbf{D}^{-1} \boldsymbol{\Phi} (\mathbf{Q} + \boldsymbol{\Phi}^T \mathbf{D}^{-1} \boldsymbol{\Phi})^{-1}) + \|\Lambda \circ \mathbf{Q}\|_1. \quad (7)$$

Once the matrices  $\boldsymbol{\Phi}^T \mathbf{D}^{-1} \boldsymbol{\Phi}$  and  $\boldsymbol{\Phi}^T \mathbf{D}^{-1} \mathbf{S} \mathbf{D}^{-1} \boldsymbol{\Phi}$  are computed, evaluating (7) only requires Cholesky decompositions in the dimension  $pL$ , so we can reduce likelihood evaluations to

$\mathcal{O}(p^3 L^3)$ . However, (7) is nonsmooth and nonconvex with respect to  $\mathbf{Q}$ , so the minimization problem is nontrivial.

Studying the convexity/concavity structure of (7) suggests a difference-of-convex (DC) algorithm where the next guess for  $\mathbf{Q}$  is obtained by solving a convex optimization problem with the concave part linearized at the previous guess. Such an algorithm reads

$$\mathbf{Q}^{(j+1)} = \arg \min_{\mathbf{Q} \succeq 0} \left( -\log \det \mathbf{Q} + \text{tr} \left( \Psi^{(j)} \mathbf{Q} \right) + \|\Lambda \circ \mathbf{Q}\|_1 \right) \quad (8)$$

where the linearization matrix

$$\Psi^{(j)} = (\mathbf{Q}^{(j)} + \Phi^T \mathbf{D}^{-1} \Phi)^{-1} + (\mathbf{Q}^{(j)} + \Phi^T \mathbf{D}^{-1} \Phi)^{-1} \Phi^T \mathbf{D}^{-1} \mathbf{S} \mathbf{D}^{-1} \Phi (\mathbf{Q}^{(j)} + \Phi^T \mathbf{D}^{-1} \Phi)^{-1} \quad (9)$$

is a function of the previous guess  $\mathbf{Q}^{(j)}$  and the aforementioned precomputed matrices. Since a DC algorithm such as (8) is a majorization-minimization algorithm, we are guaranteed that the guesses for  $\mathbf{Q}$  create a nonincreasing sequence in the objective function (7). Moreover, (8) is a well-studied problem known as the graphical lasso. Typically, the graphical lasso uses the sample covariance matrix of directly-observed, nonnoisy variables to produce a sparse inverse covariance matrix and accordingly a graphical model for the variables. Here we iteratively call the graphical lasso algorithm to estimate a graph for latent basis weights (with additive noise in the observational model), and the linearization matrix (9) acts as the sample covariance in the algorithm. We solve the graphical lasso with the second order method QUIC (Hsieh et al., 2014b).

## 2.2 Multivariate Basis Graphical Lasso

Although the previous section shows that the BGL can be readily extended to the multivariate setting, the generalization is not well-motivated by a connection to standard multivariate spatial models, and moreover it will require burdensome matrix calculations in the dimension  $pL$ . In particular, the BGL must compute the linearization matrix (9) and substitute it into the graphical lasso at each step of the DC algorithm. With our climate data example we use  $L = 2000$  basis functions and  $p = 40$  variables; an 80,000 dimensional precision matrix is too large for this procedure. Advances in graphical modeling (Fattahi et al., 2019) may allow for estimation of graphs of this magnitude, but storing the dense linearization matrix

poses an issue to further scalability. We conclude the paper with more commentary about this direct generalization (see Section 5), but here we propose a similar DC algorithm which is more feasible in a highly multivariate setting.

Our basic model still follows a penalized likelihood-based framework, minimizing

$$\hat{\mathbf{Q}} \in \arg \min_{\mathbf{Q} \succeq 0} \log \det(\mathbf{\Phi} \mathbf{Q}^{-1} \mathbf{\Phi}^T + \mathbf{D}) + \text{tr}(\mathbf{S}(\mathbf{\Phi} \mathbf{Q}^{-1} \mathbf{\Phi}^T + \mathbf{D})^{-1}) + P(\mathbf{Q}) \quad (10)$$

for some penalty  $P$ . However, an  $\ell_1$  graphical lasso-type penalty by itself does not impose any regularity on the *structure* of coefficient graphs. To motivate our proposal, we recall some recent insights into multivariate modeling that will suggest an appropriate form for  $P$ .

The multivariate spectral representation theorem states

$$\mathbf{Z}(\mathbf{s}) = \int \exp(i\boldsymbol{\omega}^T \mathbf{s}) \mathbf{W}(d\boldsymbol{\omega}) \quad (11)$$

for a mean zero stationary process  $\mathbf{Z}(\mathbf{s})$ , where  $\mathbf{W}(\cdot)$  is a complex-valued mean zero random measure vector (Stein, 1999). Taking a discretization of the integral we approximate

$$\int \exp(i\boldsymbol{\omega}^T \mathbf{s}) \mathbf{W}(d\boldsymbol{\omega}) \approx \sum_{\ell} \cos(\boldsymbol{\omega}_{\ell}^T \mathbf{s} + \theta_{\ell}) \mathbf{W}_{\ell} \quad (12)$$

to motivate writing (3) as a linear combination of *independent* random vectors  $\mathbf{W}_{\ell}$ . The representation theorem is intimately linked to the spectral density matrix of  $\mathbf{Z}(\mathbf{s})$  where we identify  $\text{Var}(\mathbf{W}_{\ell})$  with  $\mathbf{f}(\boldsymbol{\omega}_{\ell})$ . One connection to our model is that  $\mathbf{Q}_{\ell}^{-1}$  can be viewed as the spectral density matrix at frequency  $\boldsymbol{\omega}_{\ell}$ , but our approach estimates the *inverse* spectral density matrix in a Gaussian graphical framework, and moreover we will relax the tie to harmonic basis functions. Indeed, Kleiber (2017) provides interpretation and exploration of spectral coherence that will additionally motivate our penalized likelihood implementation. Before moving on, it is important to note that although we use the spectral representation theorem (11) to motivate the ensuing approach, our method is general and extends beyond harmonic basis expansions but with similar coherence-like interpretations of coefficient dependence. Guinness (2018) proposes a multivariate space-time model with flexible coherence structures which uses LMC in the spectral domain, but the covariance structure is stationary and the method is only viable for gridded data.

The multivariate basis graphical lasso model can be motivated with the same penalized likelihood context as in Section 2.1. Recall the model setup: we work under the additive model (1) with  $\mathbf{Z}(\mathbf{s})$  specified as in the basis representation (3), and  $\mathbf{W}_i$  and  $\mathbf{W}_j$  are independent Gaussian graphical vectors for  $i \neq j$ . In particular, we assume that  $\mathbf{Q}_\ell = \text{Var}(\mathbf{W}_\ell)^{-1}$  is a sparse matrix defining a graphical structure at level  $\ell$ . If we consider each  $\mathbf{Q}_\ell$  to correspond to an arbitrary sparse graphical model, then we propose  $P$  as a graphical lasso regularization for each level:

$$P(\mathbf{Q}_1, \dots, \mathbf{Q}_L) = \lambda \sum_{\ell=1}^L \sum_{i \neq j} |(\mathbf{Q}_\ell)_{ij}|. \quad (13)$$

This penalty enforces sparsity for each precision matrix but not necessarily any similarity between levels of resolution. Recent development in spectral coherence (Kleiber, 2017) suggests that we should expect the coherence of processes arising in practice to vary smoothly across levels. In addition to the  $\ell_1$  sparsity penalty, we include an  $\ell_1$  sequentially-fused penalty to encourage similarity of the conditional independence structure across adjacent levels of resolution:

$$P(\mathbf{Q}_1, \dots, \mathbf{Q}_L) = \lambda \sum_{\ell=1}^L \sum_{i \neq j} |(\mathbf{Q}_\ell)_{ij}| + \rho \sum_{\ell=1}^{L-1} \sum_{i \neq j} |(\mathbf{Q}_\ell)_{ij} - (\mathbf{Q}_{\ell+1})_{ij}|. \quad (14)$$

The new fusion penalty with tuning parameter  $\rho$  penalizes precision matrices at adjacent levels if their off-diagonals do not have the same value. This formulation suggests a smoothly-varying graph structure and produces a parsimonious conditional independence structure of the random weights over all levels of resolution.

Assuming that  $\mathbf{Q} = \text{diag}(\mathbf{Q}_1, \dots, \mathbf{Q}_L)$  does not change any reasoning leading to the BGL formulation from Section 2.1 but allows us to reduce computations on matrices of size  $pL \times pL$  to computations on  $L$   $p \times p$  matrices. At each step of the DC algorithm (8), we simplify the minimization problem to

$$\arg \min_{\mathbf{Q}_\ell \succeq 0, \ell=1, \dots, L} \left( \sum_{\ell=1}^L -\log \det \mathbf{Q}_\ell + \text{tr}(\mathbf{\Psi}_\ell \mathbf{Q}_\ell) \right) + P(\mathbf{Q}_1, \dots, \mathbf{Q}_L) \quad (15)$$

where  $\mathbf{\Psi}_\ell$  is the  $\ell^{\text{th}}$  block diagonal of the linearization matrix  $\mathbf{\Psi}$ , which depends upon the previous graph guesses. An efficient way to calculate  $\mathbf{\Psi}_1, \dots, \mathbf{\Psi}_L$  for orthogonal bases is presented in Section 3.

Using only the sparsity penalty (13) means (15) separates into  $L$  independent graphical lasso problems with “sample covariance” matrices  $\Psi_1, \dots, \Psi_L$ .<sup>1</sup> Using the fusion penalty (14) gives no such separation of (15) into  $L$  independent optimization problems at each DC iteration. Instead, we treat  $\Psi_1, \dots, \Psi_L$  as an array of sample covariance matrices and substitute them into the fused multiple graphical lasso (FMGL) (Yang et al., 2015) for modeling multiple similar graphical models across multiple datasets. A related idea is the joint graphical lasso (Danaher et al., 2014), but their similarity-inducing regularization term penalizes all pairs of graphs rather than just adjacent graphs as in (14), suggesting behavior similar to white noise processes—an unreasonable assumption for most real spatial data applications. The associated algorithm uses a slower optimization approach which calculates eigendecompositions in R. The FMGL algorithm, written in Matlab, uses the same second order approximation as QUIC (Hsieh et al., 2014b) and also exhibits quadratic convergence. A general framework for second order optimization in high dimensional statistical modeling with regularization is developed in Hsieh et al. (2014a).

### 3 Implementation Strategy

We highlight some important aspects of implementing the multivariate BGL model. In practice, we independently estimate an error variance for each variable and define the diagonal matrix  $\mathbf{D}$  accordingly.<sup>2</sup> Matrices  $\Phi^T \mathbf{D}^{-1} \Phi$  and  $\Phi^T \mathbf{D}^{-1} \mathbf{S} \mathbf{D}^{-1} \Phi$  must be computed effectively—ignoring  $\mathbf{D}^{-1}$ , the naive matrix multiplications cost  $\mathcal{O}(p^3 n L^2)$  and  $\mathcal{O}(p^3 n^2 L)$ , respectively. Moreover, the block diagonals of the linearization (9) must be retrieved without expending  $\mathcal{O}(p^3 L^3)$  flops for the matrix inverse  $(\mathbf{Q} + \Phi^T \mathbf{D}^{-1} \Phi)^{-1}$ . In Krock et al. (2020) with  $p = 1$  this linearization step was not an issue—the computational bottleneck was iteratively solving the graphical lasso in the dimension of the basis functions  $L$ . Here, we are modeling  $L$  graphs of dimension  $p$ , so the graphical modeling step may no longer be the bottleneck but rather the linearization (9). However, assuming that  $\mathbf{Q}$  is block diagonal and basis functions are orthogonal makes this linearization step trivial.

---

<sup>1</sup>See Section 3.0.1.

<sup>2</sup>See Section 3.2.

Let  $\Phi$  be the  $n \times L$  basis matrix with  $(i, j)$  entry  $\phi_j(\mathbf{s}_i)$ . Observe that

$$\mathbf{Z}(\mathbf{s}_i) = \sum_{\ell=1}^L \phi_\ell(\mathbf{s}_i) \mathbf{W}_\ell = \mathbf{M} \Phi_i^T \quad (i = 1, \dots, n) \quad (16)$$

where  $\mathbf{M}$  has columns  $\mathbf{W}_1, \dots, \mathbf{W}_L$  and  $\Phi_i^T$  is the  $i^{\text{th}}$  column of  $\Phi^T$ . Introducing the  $\text{vec}(\cdot)$  operator, which stacks the columns of a matrix one-by-one into a vector, we write the process observation vector as

$$\mathbf{Z} = \begin{pmatrix} \mathbf{Z}(\mathbf{s}_1) \\ \vdots \\ \mathbf{Z}(\mathbf{s}_n) \end{pmatrix} = \begin{pmatrix} \mathbf{M} \Phi_1^T \\ \vdots \\ \mathbf{M} \Phi_n^T \end{pmatrix} = \text{vec}(\mathbf{M} \Phi^T) \quad (17)$$

where the last equation follows from (16.2.7) in Harville (1997). The  $\text{vec}$  operator cooperates with the Kronecker product  $\otimes$  in the following way:  $\text{vec}(ABC) = (C^T \otimes A) \text{vec}(B)$  whenever  $ABC$  is well-defined. For us, this implies

$$\mathbf{Z} = (\Phi \otimes I_p) \mathbf{W} \quad (18)$$

since  $\mathbf{W} = \text{vec}(\mathbf{M})$  by construction. Thus we identify  $\Phi = \Phi \otimes I_p$ . Also note that  $\mathbf{D}^{-1} = I_n \otimes \text{diag}(\tau_1^{-2}, \dots, \tau_p^{-2})$  is a Kronecker product. Since  $(A \otimes C)(B \otimes D) = AB \otimes CD$  whenever  $AB$  and  $CD$  are well-defined, we have the Kronecker product representation  $\Phi^T \mathbf{D}^{-1} \Phi = \Phi^T \Phi \otimes \text{diag}(\tau_1^{-2}, \dots, \tau_p^{-2})$ , which will be sparse for any choice of basis functions. In general, solving systems with  $\mathbf{Q} + \Phi^T \mathbf{D}^{-1} \Phi$  does not have an exploitable structure since  $\mathbf{Q}$  is block diagonal yet  $\Phi^T \mathbf{D}^{-1} \Phi$  is a Kronecker product. However, using orthogonal basis functions (i.e.,  $\Phi^T \Phi = I_L$ ) means that  $\Phi^T \mathbf{D}^{-1} \Phi$  is diagonal, so the first term in (9) is block diagonal and can be easily inverted in  $\mathcal{O}(Lp^3)$ .

The linearization also involves  $\Phi^T \mathbf{D}^{-1} \mathbf{S} \mathbf{D}^{-1} \Phi = (\Phi^T \mathbf{D}^{-1} \mathbf{Y}_{\text{data}})(\mathbf{Y}_{\text{data}}^T \mathbf{D}^{-1} \Phi)/m$ , where  $\mathbf{Y}_{\text{data}}$  is the data matrix with columns of realizations  $\mathbf{Y}_1, \dots, \mathbf{Y}_m$ . Using  $\text{vec}(ABC) = (C^T \otimes A) \text{vec}(B)$  again,

$$\Phi^T \mathbf{D}^{-1} \mathbf{Y}_i = \text{vec}(\text{diag}(\tau_1^{-2}, \dots, \tau_p^{-2}) \text{mat}(\mathbf{Y}_i) \Phi) \quad (19)$$

where  $\text{mat}(\mathbf{Y}_i)$  is the  $p \times n$  matrix with  $\text{vec}(\text{mat}(\mathbf{Y}_i)) = \mathbf{Y}_i$ . So  $\Phi^T \mathbf{D}^{-1} \mathbf{Y}_{\text{data}}$  can be calculated in  $\mathcal{O}(mnpL)$  and has low storage cost  $\mathcal{O}(mpL)$ . Once  $\Phi^T \mathbf{D}^{-1} \mathbf{Y}_{\text{data}}$  and the block

diagonals of  $(\mathbf{Q} + \Phi^T \mathbf{D}^{-1} \Phi)^{-1}$  are computed, the block diagonals of the second term in (9) can be computed in  $\mathcal{O}(Lp^2m)$ .

To summarize, for an orthogonal basis, only  $\{\mathbf{Q}_1, \dots, \mathbf{Q}_L\}$ ,  $\{\tau_1^{-2}, \dots, \tau_p^{-2}\}$ , and  $\Phi^T \mathbf{D}^{-1} \mathbf{Y}_{\text{data}}$  must be stored in memory, and we can compute the block diagonals of (9) in  $\mathcal{O}(Lp^3 + Lp^2m)$ . These  $L$   $p \times p$  block matrices are then sent into the FMGL as an array of  $L$  “sample covariance” matrices, and the solution to the FMGL problem is the next guess for  $\{\mathbf{Q}_1, \dots, \mathbf{Q}_L\}$ , and the entire procedure is repeated until  $\|\mathbf{Q}^{(j+1)} - \mathbf{Q}^{(j)}\|_F / \|\mathbf{Q}^{(j)}\|_F < \epsilon$ , which we set as  $\epsilon = 0.05$ .

### 3.0.1 Initial Guess (Unfused Estimate)

When considering the fusion penalty, a natural initial guess is the corresponding unfused estimate. With  $\rho = 0$ , the main optimization (15) amounts to solving the graphical lasso independently by level:

$$\arg \min_{\mathbf{Q}_\ell \succeq 0, \ell=1, \dots, L} \left( \sum_{\ell=1}^L -\log \det \mathbf{Q}_\ell + \text{tr}(\Psi_\ell \mathbf{Q}_\ell) + \lambda \sum_{i \neq j} |(\mathbf{Q}_\ell)_{ij}| \right). \quad (20)$$

The entire algorithm has linear complexity and storage in  $L$  in this case.

## 3.1 Maximum Likelihood Estimate

It is also easy to obtain the unpenalized maximum likelihood estimates for  $\mathbf{Q}_1, \dots, \mathbf{Q}_L$ . Recall that  $S^{-1} = \arg \min_{Q \succeq 0} -\log \det Q + \text{tr}(SQ)$ , assuming  $S$  is nonsingular. This means that our DC algorithm would simply invert the linearization matrix (or each block diagonal of the linearization matrix in the multivariate case) rather than substitute it into the graphical lasso. Again,  $\mathbf{Q}_1, \dots, \mathbf{Q}_L$  are independent, which implies the same storage and complexity as the unfused estimate in Section 3.0.1. This algorithm takes many more DC iterations to converge than either of the regularized estimates.



### 3.2 Estimating the Error Variances

Given a single variable with sample covariance  $S$ , we minimize the following function jointly over  $\tau^2$  and a few parameters describing a diagonal matrix  $Q$ :

$$\log \det (Q + \tau^{-2} \Phi^T \Phi) - \log \det Q - \text{tr} \left( \tau^{-4} \Phi^T S \Phi (Q + \tau^{-2} \Phi^T \Phi)^{-1} \right) + n \log \tau^2 + \tau^{-2} \text{tr}(S).$$

Note that this expression can be simplified with orthogonal bases, and the trace terms can be quickly computed as squared Frobenius norms. The diagonal parameterization of  $Q$  and parameter estimation is further discussed in Section 4.1. We record values for  $\tau_1^2, \dots, \tau_p^2$  in Table 2 in the Appendix which are used throughout the rest of the paper. A similar approach used in Krock et al. (2020) was found to be successful in recovering error variances even with a misspecified spatial covariance structure.

### 3.3 Cross-Validation

First we describe the cross-validation procedure for a pair of penalty parameters  $(\lambda, \rho)$ . Suppose we use  $k$  folds and consider  $t$  arbitrary pairs of penalties represented by  $\{\Lambda_1, \dots, \Lambda_t\}$ . Let  $\hat{Q}_{\Lambda_j}(\mathbf{S})$  be the estimate we get from applying our algorithm with empirical covariance  $\mathbf{S} = \frac{1}{m} \sum_{i=1}^m \mathbf{Y}_i \mathbf{Y}_i^T$  and penalty pair  $\Lambda_j$ . For  $A \subseteq \{1, \dots, m\}$ , let  $\mathbf{S}_A = |A|^{-1} \sum_{i \in A} \mathbf{Y}_i \mathbf{Y}_i^T$ . We seek  $\Lambda$  so that  $\alpha(\Lambda) = \ell(\hat{\mathbf{Q}}_{\Lambda}(\mathbf{S}), \mathbf{S})$  is small, where

$$\ell(\mathbf{Q}, \mathbf{S}) = \log \det (\mathbf{Q} + \Phi^T \mathbf{D}^{-1} \Phi) - \log \det \mathbf{Q} - \text{tr} (\Phi^T \mathbf{D}^{-1} \mathbf{S} \mathbf{D}^{-1} \Phi (\mathbf{Q} + \Phi^T \mathbf{D}^{-1} \Phi)^{-1}) \quad (21)$$

is the unpenalized likelihood function in (7). The cross-validation approach is to partition

$\{1, \dots, m\}$  into disjoint sets  $\{A_1, \dots, A_k\}$  and select  $\hat{\Lambda} = \arg \min_{\Lambda \in \{\Lambda_1, \dots, \Lambda_t\}} \hat{\alpha}(\Lambda)$  where

$$\hat{\alpha}(\Lambda) = k^{-1} \sum_{i=1}^k \ell(\hat{\mathbf{Q}}_{\Lambda}(\mathbf{S}_{A_i^c}), \mathbf{S}_{A_i}).$$

Jointly searching over  $\lambda$  and  $\rho$  can quickly become unwieldy even when considering a small combination of sparsity and fusion penalties, as noted by Danaher et al. (2014), who instead suggest a dense search for  $\lambda$  with  $\rho = 0$  fixed and then a search for  $\rho$  with that sparsity value fixed. The individual cross-validation for either  $\lambda$  or  $\rho$  follows the same idea: whichever penalty parameter has the lowest negative log-likelihood average across folds is selected.

## 4 Data Analysis

This section is broken into two main, but related, application and validation efforts. Both are done with the lens of the climate data problem: we begin with some exploratory analyses of the climate dataset, deriving reasonable basis functions and providing discussion to guide intuition for the ensuing model application. The second section is a detailed simulation study that tests our ability, under a similar setup as the climate example, to recover meaningful and relevant graphs for coefficients at different levels of basis functions under realistic assumptions on possible graph structures. The final section provides the full analysis of our model on the Community Atmosphere Model (CAM) data along with scientific interpretations of recovered graphical structures and some implied covariance and cross-covariance patterns.

### 4.1 Data Description and Exploratory Analyses

We apply our method to a large climatological dataset from an ensemble study conducted at the National Center for Atmospheric Research (NCAR). Climate variability is typically assessed by examining a collection of numerical climate model simulations, which are computationally and economically expensive to produce. Relationships between variables at different spatial scales are crucial for scientific investigations; hence a scalable statistical model which can simulate multivariate processes could be a powerful tool for climatologists. Our method allows for efficient emulation and straightforward interpretation of complex geophysical model variable relationships potentially filling this niche.

A climate model ensemble is typically a collection of climate simulations from the same numerical model using various initial conditions; ours is an extended version of the ensemble described in Baker et al. (2015) with  $m = 343$  members. Data are recorded at  $n = 48,602$  gridded spatial locations over the globe. There are a total of 164 variables available, the majority of which are three-dimensional, meaning they have a third dimension corresponding to 30 vertical atmospheric levels. For our study we only consider the two-dimensional surface variables, and a subset thereof. First, the variables are on different scales, so they are standardized with a pixelwise empirical mean and pixelwise empirical standard deviation. Histograms and Q-Q plots were consulted to remove strongly non-normal variables. Note

that our data are yearly-averaged quantities, so a Gaussian assumption is generally reasonable. Potential variables were also removed if they were very strongly correlated, suggesting redundant information (e.g., when vectorized across space and realizations, the absolute correlation between two processes was above 0.9). We settled upon the  $p = 40$  variables listed in Table 1, which are grouped into five categories: aerosol variables, cloud variables, flux variables, precipitation variables, and transport/state variables. Throughout the rest of the document, aerosol variables are colored red, cloud variables are colored blue, flux variables are colored green, precipitation variables are colored purple, and transport/state variables are colored grey.

With the  $p = 40$  variables in hand, our approach relies on first specifying a set of spatial basis functions. We construct such functions as empirical orthogonal functions (EOFs) (Wikle, 2010), which are widely used in the atmospheric and climate sciences. Typically, EOFs are used in a temporal context with a single variable. Let's consider a single spatiotemporal variable and suppose we have a matrix  $B$  of data with rows indexing  $n$  spatial locations and columns indexing  $t$  time points. If  $B = UDV^T$  is the (economy) SVD of the data matrix, the columns of the orthogonal matrix  $U$ , referred to as EOFs, represent the normalized eigenvectors of the process empirical covariance matrix  $BB^T$ .

We compute the (economy) SVD of the  $n \times pm = 48,602 \times 13,720$  data matrix where a row corresponds to a spatial location and contains the  $p$  standardized variables ordered sequentially by realization. Such an approach can be thought of as generating *pooled* EOFs that describe common structure seen amongst all variables. Using the same notation  $UDV^T$  for the SVD, we follow common practice and take the first  $L$  columns of  $U$  to form our  $n \times L$  basis matrix  $\Phi$ . Exploratory analysis suggests truncating after  $L = 2000$  EOFs is a reasonable tradeoff between using a relatively small number of basis functions and explaining sufficient variance (97.2%). The first two pooled EOFs are displayed in Figure 1. We emphasize that pooling variables together to create EOFs is nontraditional and explains why the first two EOFs account for such little variability.

With this formulation it is important to clarify the role of the additive error term. Here an interpretation as a traditional spatial statistical nugget effect is not well-motivated and instead we think of  $\varepsilon$  as a fine-scale process which is at smaller scale than the EOFs and

Variable	Description	Units	Category
AODVIS	Aerosol optical depth	550 nm	Aerosol
BURDEN1	Aerosol burden mode 1	kg/m <sup>2</sup>	Aerosol
BURDEN2	Aerosol burden mode 2	kg/m <sup>2</sup>	Aerosol
BURDEN3	Aerosol burden mode 3	kg/m <sup>2</sup>	Aerosol
BURDENBC	Black carbon aerosol burden	kg/m <sup>2</sup>	Aerosol
BURDENPOM	POM aerosol burden	kg/m <sup>2</sup>	Aerosol
BURDENSEASALT	Seasalt aerosol burden	kg/m <sup>2</sup>	Aerosol
BURDENSO4	Sulfate aerosol burden	kg/m <sup>2</sup>	Aerosol
BURDENSOA	SOA aerosol burden	kg/m <sup>2</sup>	Aerosol
CDNUMC	Vertically-integrated droplet concentration	1/m <sup>2</sup>	Cloud
CLDHGH	Vertically-integrated high cloud	fraction	Cloud
CLDMED	Vertically-integrated mid-level cloud	fraction	Cloud
CLDTOT	Vertically-integrated total cloud	fraction	Cloud
FLDS	Downwelling longwave flux at surface	W/m <sup>2</sup>	Flux
FLNS	Net longwave flux at surface	W/m <sup>2</sup>	Flux
FLNSC	Clearsky net longwave flux at surface	W/m <sup>2</sup>	Flux
FLNT	Net longwave flux at top of model	W/m <sup>2</sup>	Flux
FLNTC	Clearsky net longwave flux at top of model	W/m <sup>2</sup>	Flux
FSDS	Downwelling solar flux at surface	W/m <sup>2</sup>	Flux
FSDSC	Clearsky downwelling solar flux at surface	W/m <sup>2</sup>	Flux
FSNS	Net solar flux at surface	W/m <sup>2</sup>	Flux
FSNSC	Clearsky net solar flux at surface	W/m <sup>2</sup>	Flux
FSNTC	Clearsky net solar flux at top of model	W/m <sup>2</sup>	Flux
FSNTOA	Net solar flux at top of atmosphere	W/m <sup>2</sup>	Flux
LHFLX	Surface latent heat flux	W/m <sup>2</sup>	Flux
LWCF	Longwave cloud forcing	W/m <sup>2</sup>	Cloud
PBLH	PBL height	W/m <sup>2</sup>	Transport/State
PS	Surface pressure	Pa	Transport/State
QREFHT	Reference height humidity	kg/kg	Precipitation
SHFLX	Surface sensible heat flux	W/m <sup>2</sup>	Flux
SWCF	Shortwave cloud forcing	W/m <sup>2</sup>	Cloud
TAUX	Zonal surface stress	N/m <sup>2</sup>	Transport/State
TAUY	Meridional surface stress	N/m <sup>2</sup>	Transport/State
TGCLDCWP	Total grid-box cloud water path (liquid and ice)	kg/m <sup>2</sup>	Cloud
TGCLDIWP	Total grid-box cloud ice water path	kg/m <sup>2</sup>	Cloud
TGCLDLWP	Total grid-box cloud liquid water path	kg/m <sup>2</sup>	Cloud
TMQ	Total vertically integrated precipitable water	kg/m <sup>2</sup>	Precipitation
TREFHT	Surface air temperature at reference height	K	Transport/State
U10	10m wind speed	m/s	Transport/State
PRECT	PRECL Large-scale (stable) precipitation rate (liq + ice) plus PRECC Convective precipitation rate (liq + ice)	m/s	Precipitation

Table 1: Variable descriptions. Note that analysis happens on standardized, unitless data.

absorbs the remaining variability unexplained by the pooling of variables. As noted in Wikle (2010), if enough eigenvectors are used to explain sufficient variation, then it is reasonable to assume that the EOF residuals are uncorrelated in space. This motivates the white

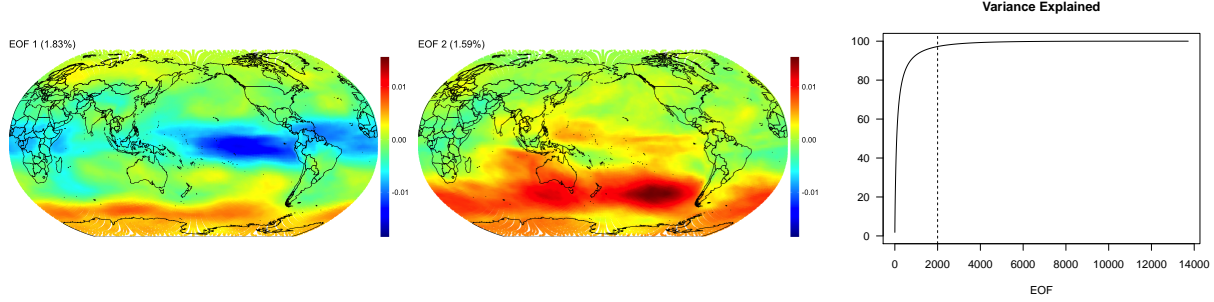


Figure 1: First two pooled EOFs of the standardized CAM data. The two EOFs account for 1.83% and 1.59% of the total variability of all 40 variables, respectively. Rightmost plot shows the cumulative percentage of variability explained by the EOFs, with  $L = 2000$  EOFs capturing 97.2% of the total variance.

noise assumption on  $\epsilon$  which in turn suggests independently estimating  $\tau_1^2, \dots, \tau_p^2$  using the procedure described in Section 3.2. Namely, for each variable, we optimize the likelihood in Section 3.2 over two parameters  $(\psi^2, \tau^2)$  under the assumption that the precision matrix has constant diagonal  $\psi^2$ . We also tried a similar diagonal assumption on the precision matrix but where the diagonal grows exponentially with  $\ell^{\text{th}}$  element  $\psi^2 e^{\alpha \ell}$ . An exponential parameterization reflects the fact that we expect smaller marginal precision values (i.e., higher variance) at lower levels of resolution and larger marginal precision values (i.e., lower variances) at higher frequencies. These low dimensional optimization problems are solved with a standard L-BFGS algorithm. Values are shown in Table 2 in the Appendix along with a signal-to-noise ratio. The sum of the diagonal of  $Q^{-1}$  gives a quantification of the total signal variance, and we divide this by  $\tau^2$  to get the signal-to-noise ratio  $\eta = \frac{\psi^{-2} \sum_{\ell=1}^L (e^{-\alpha})^\ell}{\tau^2}$ . In the case where  $Q$  has a constant diagonal  $\psi^2$ , the ratio is  $\eta = \frac{L\psi^{-2}}{\tau^2}$ .

Figure 2(a) compares the estimated signal-to-noise ratio for the two types of diagonal  $Q$ . Results suggest that the constant diagonal explains more of the signal, which is somewhat counterintuitive. This result makes sense with respect to the formulas for  $\eta$  shown above, assuming  $\psi^{-2}$  and  $\tau^2$  are equal, since  $\sum_{\ell=1}^L (e^{-\alpha})^\ell < L$  when  $\alpha > 0$ . Estimates for  $\tau^2$  are indeed the same out to several decimal places, but estimates for  $\psi^{-2}$  are about four times smaller in the constant diagonal case (see Table 2). Our explanation is that the constant diagonal gives a smaller precision (higher variance) at higher frequencies than the exponential diagonal, hence the larger signal-to-noise ratio. Interesting patterns among the

variables emerge in both plots in Figure 2. Many of the aerosol or cloud variables appear to be clustered together, and the pressure variable seems to be noticeably smoother than the rest, which is physically expected and visually the case when examining model output.

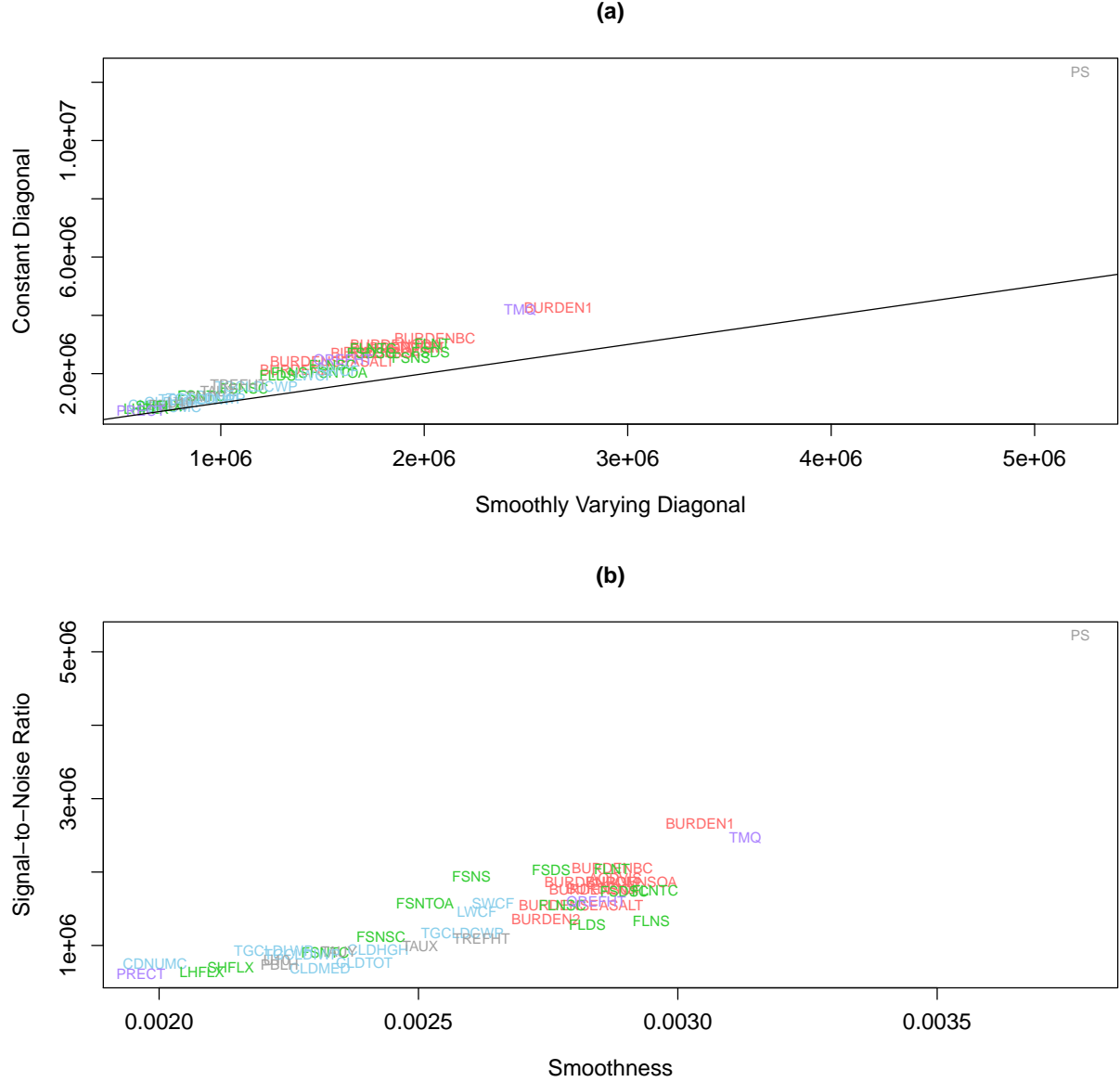


Figure 2: (a) compares signal-to-noise ratio under the two diagonal  $Q$  parameterizations. Line in (a) has slope one and passes through the origin. (b) compares smoothness  $\alpha$  and signal-to-noise ratio  $\eta$  for the variables. See values in Table 2 in the Appendix.

## 4.2 Simulation Study

This section is dedicated to a simulation study that aims to approximate the behavior we expect to see in the actual climate data analysis. Our goal is to determine the ability of our estimation approach to recover meaningful and correct graphical structures from data simulated under the same setup as the available CAM data, as well as assess the cross-validation scheme. In particular, we simulate from the model using the basis functions  $\phi_1, \dots, \phi_L$  and error variances  $\tau_1^2, \dots, \tau_p^2$  described in the previous section with the same number of variables, ensemble members, and spatial locations as in CAM.

A main question is what graphs  $\mathbf{Q}_1, \dots, \mathbf{Q}_L$  to simulate from. The study is broken into two main pieces: the first is a case where all coefficient vectors have the same precision matrix; such an approach can be interpreted as approximating a multivariate white noise process. The second approach is more realistic, in which processes are constructed using values in Table 2 to mimic smoothnesses that are exhibited in the actual dataset. Both options, described in more detail below, are governed by an initial precision matrix  $\mathbf{Q}_0$ .

- (a) White noise: each level of resolution has the same graph;  $\mathbf{Q}_0 = \mathbf{Q}_1 = \mathbf{Q}_2 = \dots = \mathbf{Q}_L$ .
- (b) Spatially correlated: at each level  $\ell$  the coefficients of the basis functions are generated according to the Hadamard product covariance model  $(s_\ell s_\ell^T) \circ \mathbf{Q}_0^{-1}$  where  $s_\ell = (\psi_1^{-1} e^{-\alpha_1 \ell/2}, \dots, \psi_p^{-1} e^{-\alpha_p \ell/2})^T$  and the smoothness parameters  $(\alpha_1, \dots, \alpha_p)$  and standard deviations  $(\psi_1, \dots, \psi_p)$  are from Table 2. This scales the processes to behave with smoothnesses and variances that are exhibited by the standardized CAM variables and also preserves the sparsity pattern of the original graph  $\mathbf{Q}_0$  across all levels.

To specify  $\mathbf{Q}_0$ , we first vectorize each variable over both space and realization and then calculate the corresponding correlation matrix. This correlation matrix, shown Figure 3(a), is substituted into the standard graphical lasso to obtain  $\mathbf{Q}_0$ . Note that the graphical lasso penalty here equals  $\xi \sum_{\ell=1}^L \sum_{i \neq j} |(\mathbf{Q}_\ell)_{ij}|$  and does not include the diagonal to be consistent with (14). To be clear, the notation  $\xi$  is used here because this is a fundamentally different problem without basis functions, but  $\xi$  plays the same role as the previous sparsity penalty parameter  $\lambda$ . After some exploratory analysis, we consider a relatively dense initial graph

corresponding to  $\xi = 0.2$ ; see an illustration in Figure 3. In each case, the setup of the simulated ensemble is the same size as the true Community Atmosphere Model: 343 ensemble members with 40 variables at 48,602 locations. To choose cross-validation parameters, we follow steps from Section 3.3 and select a sparsity penalty with  $\rho = 0$  fixed followed by a fusion penalty with the optimal sparsity penalty fixed. With the same graphical model repeated across levels, we may expect a large  $\rho$  value to be optimal. Note, however, that the diagonals in (14) are unpenalized, so  $\rho \rightarrow \infty$  does not necessarily produce identical estimates at each level.

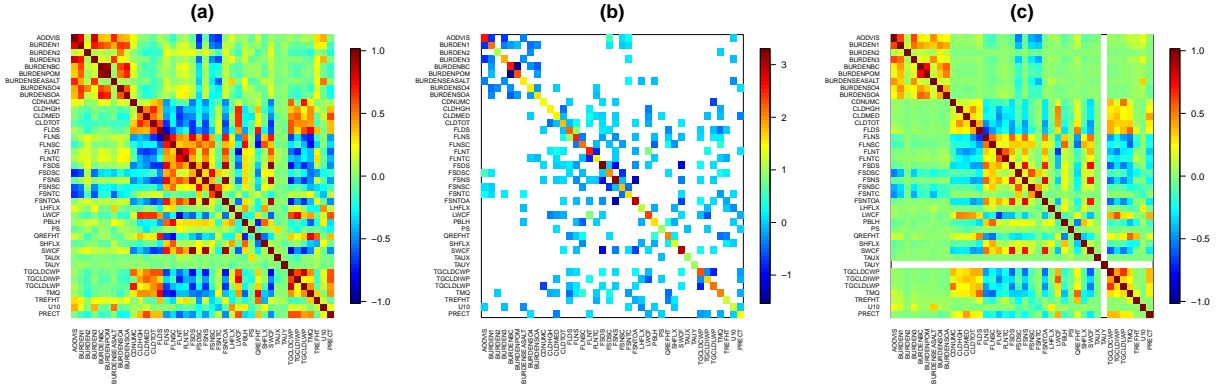


Figure 3: (a) shows the true pairwise correlations among the standardized CAM variables, taken across space and realization. (b) shows the precision matrix from substituting correlation matrix (a) into the graphical lasso problem with penalty  $\xi = 0.2$ . The resulting precision matrix (b) is 81% sparse, and its correlation matrix is shown in (c).

#### 4.2.1 Results

We show cross-validation results for the two cases and several other summarizing plots that describe the behavior of the estimated graphical models across level. Each case considered a 5-fold CV where 4/5 of the realizations were used for training and the remaining 1/5 were used for testing. Figure 4 shows cross-validation results for the sparsity parameter  $\lambda$  with  $\rho = 0$  fixed. The negative log-likelihood has a minimizer which is destroyed with the addition of the sparsity penalty (13), which is counterintuitive since we would expect the penalized likelihood to select a sparser solution. In general it is difficult to say anything about (13) as a function of  $\lambda$  since  $\|Q_\lambda\|_1$  decreases as  $\lambda$  increases. Observe that in the white noise



case (a),  $\lambda = 1$  is large enough to produce a diagonal precision matrix across all levels, as the penalized and unpenalized curves coincide. This is not the case in (b) where precision matrices grew exponentially with level instead of remaining constant; a much larger sparsity penalty is required to produce diagonal precision matrices. Similar curves to those in Figure 4 but for the fusion penalty (with optimal sparsity value  $\lambda$  fixed) were jagged and gave little insight into which  $\rho$  values from  $\{1, 2, \dots, 50\}$  were preferred.

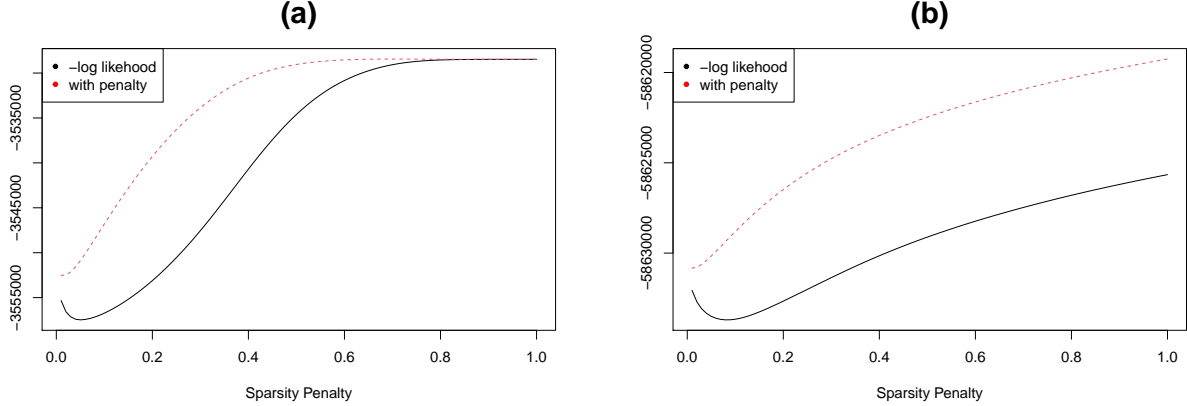


Figure 4: CV results for the sparsity penalty while  $\rho = 0$  is fixed. Red line penalizes for sparsity as in equation (13). Minimizing value is  $\lambda = 0.05$  in the white noise case (a) and  $\lambda = 0.08$  in the correlated case (b).

Figure 5 shows a count of the number of zeros in the precision matrix over level. With  $\rho$  set to zero, the correct underlying graph structure is apparent in both cases. For (a), adding a fusion penalty of  $\rho = 11$  produces the same graphical structure across all levels, while in (b), an even stronger fusion penalty  $\rho = 43$  is unable to pin down the graphical structure. This is likely due to the low sparsity penalty  $\lambda = 0.08$  which combines with the exponentially growing values in the precision matrix and large fusion penalty to incorrectly fuse graph edges across adjacent levels of resolution.

Finally, in Figure 15 in the Appendix, we display the estimated marginal precision for each variable over level. In general, we found that the marginal precisions are largely dictated by the sparsity penalty and adding a fusion penalty has little effect. For the white noise case (a), the curves appear constant across level, as expected. For case (b) where the data-generating precision matrices increase exponentially with level, the curves appear linear on a



estimate marginal precision values that were constant across level and also exponentially growing across level without making any assumptions about the behavior of these marginal precisions.

## 4.3 CAM Data Analysis

### 4.3.1 Cross-Validation Attempt

We proceed to the data analysis using the basis setup described in Section 4.1 and  $\tau_1^2, \dots, \tau_p^2$  from Table 2. The remaining question is what penalty parameters to use. We performed a 5-fold CV search over  $\lambda \in \{1, 5, 10, 15, 20, 25, \dots, 995, 1000\}$ . For each fold, the testing data was all realizations assigned to that fold (i.e.,  $1/5$  of all realizations), and the training data was the rest (i.e.,  $4/5$  of all realizations). We recorded the negative log-likelihood (i.e., (7) without the penalty) and its penalized version, but unfortunately there was little to infer from the results – both favored the lowest sparsity penalty  $\lambda = 1$ . Considering smaller sparsity values in the interval  $(0, 1)$  is an option, but this increases the computation time dramatically, unlike in the simulation study where such solutions were still computed fairly quickly.

### 4.3.2 Fixing Penalty Parameters

With this cross-validation attempt and similar difficulties with penalties encountered in Danaher et al. (2014) in mind, we proceed by fixing several penalty pairs and examining the resulting modeling implications. Ideally, we would select a model with a sensible, interpretable graphical neighbor structure over levels. Differences between models with different graph structures may be minor as different graphs can give approximately the same correlation structure.

In the supplemental material and remainder of this document, we display several results for  $\lambda = 20$  since this looked like an inflection point in a plot of  $\lambda$  versus the total graph sparsity percentage (see Figure 6(a)). The other plot in Figure 6 shows how the sparsity of the graphs corresponding to  $\lambda = 20$  changes over levels. We also will occasionally compare

$\lambda = 20$  results with those from  $\lambda = 1$  to give an idea of how the implied graph structure changes with different penalties.

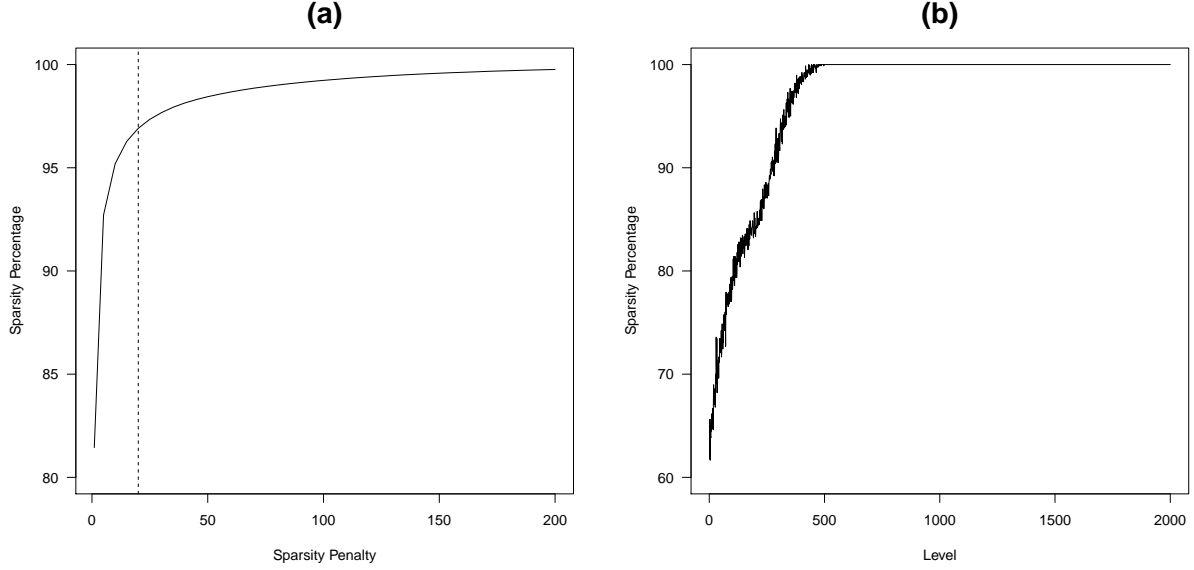


Figure 6: (a): total sparsity percentage of the graphs  $\{\mathbf{Q}_1, \dots, \mathbf{Q}_L\}$  as a function of  $\lambda$ . (b): sparsity percentage by level for  $\lambda = 20$ .

One notion of dependence we examine comes from averaging the estimated variable correlation matrix over space. To be precise, from (3) we see the process covariance matrix at location  $\mathbf{s}$  is  $\sum_{\ell=1}^L (\phi_{\ell}(\mathbf{s}))^2 (\mathbf{Q}_{\ell})^{-1}$ . This covariance matrix is converted into a correlation matrix, and the correlation matrices for each location are averaged. Figure 16 in the Appendix shows the result for the unpenalized model (i.e., the case with  $\lambda = 0$  and  $\rho = 0$  described in Section 3.1) as well as the penalized models. Different penalties produce minor differences in the implied correlation structure, but the overall similarity with Figure 3(a), which calculated variable correlations for the standardized CAM data by ignoring space and realization, suggests that our model correctly captures correlations between variables.

For the next set of model diagnostics, we turn away from correlations to look at precision matrices. Familiar plots of estimated marginal precisions by level are shown in Figure 7. Clearly, the exponential parameterization considered in the simulation study is not well-suited to our data. Just as in the simulation study, adding a sparsity penalty causes the pressure variable (colored grey) to have the highest marginal precisions at high levels of

resolution, as we would expect from the smoothest variable. Overall, adding a sparsity penalty brings all marginal precisions down by an order of magnitude, with particularly strong shrinkage at lower levels of resolution. Given the focus on regularization, these results may not seem surprising, but the diagonals of the precision matrix are not penalized in any formulation we have considered. This shrinkage of marginal precisions can be attributed to the larger number of neighbors in the low-penalized graph structures, which means that the (conditional) precision will be higher than in estimates from higher penalties.

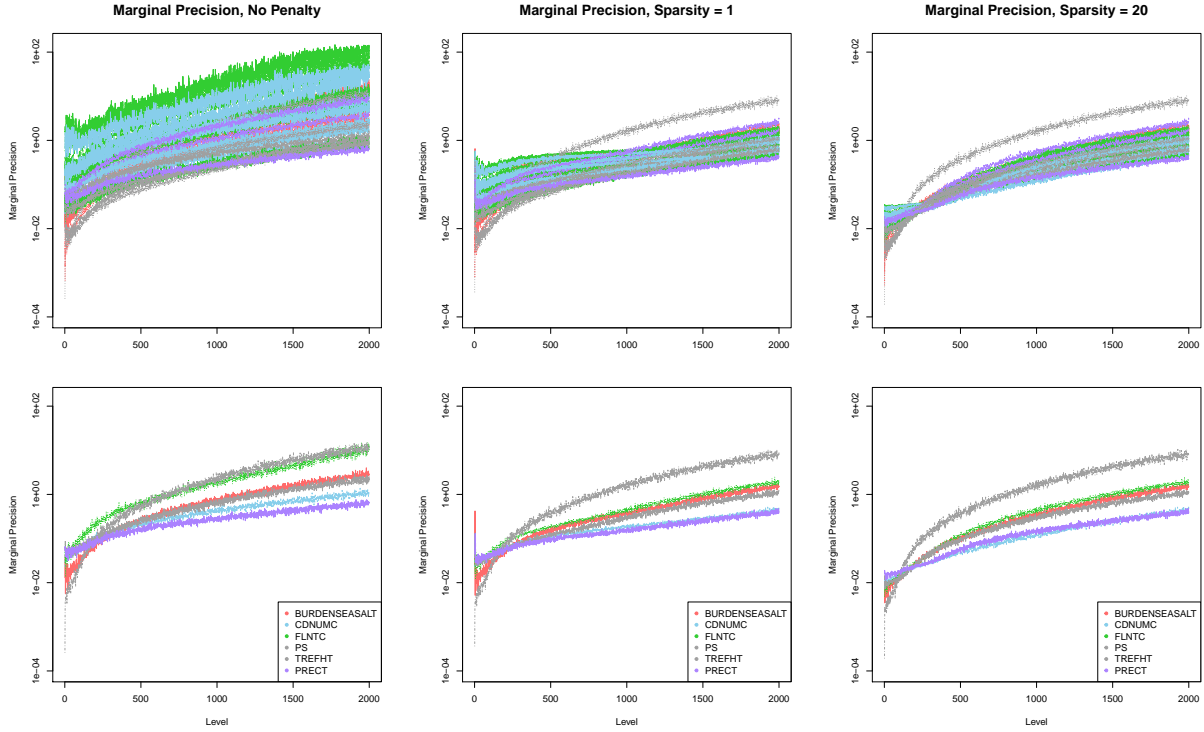


Figure 7: Marginal precision estimates (i.e., diagonals of  $\hat{\mathbf{Q}}_1, \dots, \hat{\mathbf{Q}}_{2000}$ ) shown by level for various penalty choices. Log scale on  $y$ -axis. Bottom row shows a subset of six variables from the top row. The grey pressure variable is noticeably smoother than the rest after regularization is added.

Our penalized maximum likelihood procedure produces interpretable graphical models which imply conditional independencies among the variables at varying levels of resolution. Here we study some properties of the estimated graphical models. Figure 8 gives an idea of how the conditional independence structure changes with respect to level for different penalties. The left column counts the nonzeros of the estimated precision matrices  $\hat{\mathbf{Q}}_1, \dots, \hat{\mathbf{Q}}_{2000}$

over level. With  $\lambda = 20$  we see several conditional independencies between variables that persist over all levels. The middle and right columns show how the conditional dependence neighborhood structure of two variables (BURDENSEASALT and PS) changes over level, and the impact of the fusion penalty is most apparent in these columns. Broadly speaking, the fusion penalty smooths out the neighbor pattern across levels. Note that the fusion penalty can fuse adjacent nonzeros rather than adjacent zeros and can cause a neighbor to fuse across all levels if  $\rho$  is large enough. Figure 9 displays estimated graphical models for different levels of resolution. At early levels corresponding to large scale spatial patterns, the graphs are quite dense. Higher frequency EOFs display interesting and reasonable patterns. For example, near the top of the  $\ell = 150$  graph we see groupings among many cloud and precipitation variables, and these connections are more evident at higher levels and even with different penalty parameters (not shown). For higher level EOFs, past around  $\ell = 500$  with  $\lambda = 20$ , the graphs suggest variable independence. This idea of complete independence is explored in Figure 10 where we display the first level at which each variable is independent and remains independent of all other variables. Note again a natural grouping of variable types, with transport and pressure variables achieving independence much earlier than finer-scale precipitation and cloud variables. Further, as could also be observed in the visualization of the conditional dependence structure for the two selected variables in Figure 8, the level at which independence occurs varies quite dramatically with the sparsity penalty, leading to roughly a four-fold increase in the number of connected levels going from  $\lambda = 20$  to  $\lambda = 1$ .

Now we examine some spatial properties of our estimates. Figure 11 shows the estimated local standard deviations for a subset of six variables. Recall that the variables were standardized to have an empirical unit standard deviation, so these plots should be interpreted as potential bias corrections where the standardization fails to accurately describe the variability. Most striking is the El Niño effect apparent in the plot for the pressure variable PS. The pattern’s presence is unsurprising since El Niño/La Niña are strongly tied to changes in pressure over the Pacific Ocean and their relative infrequency likely requires more modeling care than just an empirical standardization. Finer-scale variables CDNUMC and PRECT are able to capture distinct behavior in mountainous regions (e.g., Rocky Mountains and Himalayas).

In our last collection of figures, we return to correlation, but this time examine correlation over space as well as across variables. Figure 12 shows variable correlations as a function of space. To be precise, each image shows the correlation between the location marked in green and all other locations. Nonstationarity is evident from the difference in behaviors between land and ocean, and long range negative correlation is seen to be a possible byproduct of this modeling scheme. In Figure 13, we display estimated local cross-correlations between a few of our selected variables. Expected negative and positive correlations between pairs of variables are correctly captured (e.g., between pressure and precipitation and between cloud droplet concentration and precipitation). Finally, in Figure 14, we show variable cross-correlations as a function of space. To be precise, each image shows the cross-correlation between the first variable at the location marked in green and the second variable at all other locations. The flexibility of the model is again apparent in its nonstationary behavior and various positive and negative cross-correlations. Such behavior is difficult to accommodate using extant models but readily available in our approach without any additional effort (Kleiber and Genton, 2013). Both the correlation and cross-correlation functions centered where El Niño/La Niña occur (see right column in Figures 12 and 14) exhibit long-range dependence through the equator across the Pacific Ocean.

We conclude the data analysis with a brief commentary about the timing results, assuming the orthogonal basis has been constructed and  $\tau_1^2, \dots, \tau_p^2$  are estimated. Note that the latter step is fairly quick using the technique in Section 3.2 with an orthogonal basis. The choice of penalty dictates the runtime of the DC algorithm. For the maximum likelihood estimate with no penalty, the tolerance  $\epsilon = 0.05$  is reached in fifteen DC iterations in five seconds. With sparsity penalty  $\lambda = 20$ , the algorithm converges in two DC iterations in forty-five seconds. With sparsity penalty  $\lambda = 1$ , the algorithm again requires two DC iterations but takes thirteen minutes. With fusion penalty  $\rho = 10$ , both estimates converged in one DC iteration using the  $\rho = 0$  solution as the initial guess, but  $(\lambda, \rho) = (20, 10)$  took seven minutes while  $(\lambda, \rho) = (1, 10)$  took one minute. All experiments were performed in Matlab on a MacBook Pro with a 2.6 GHz Intel Core i7 processor.

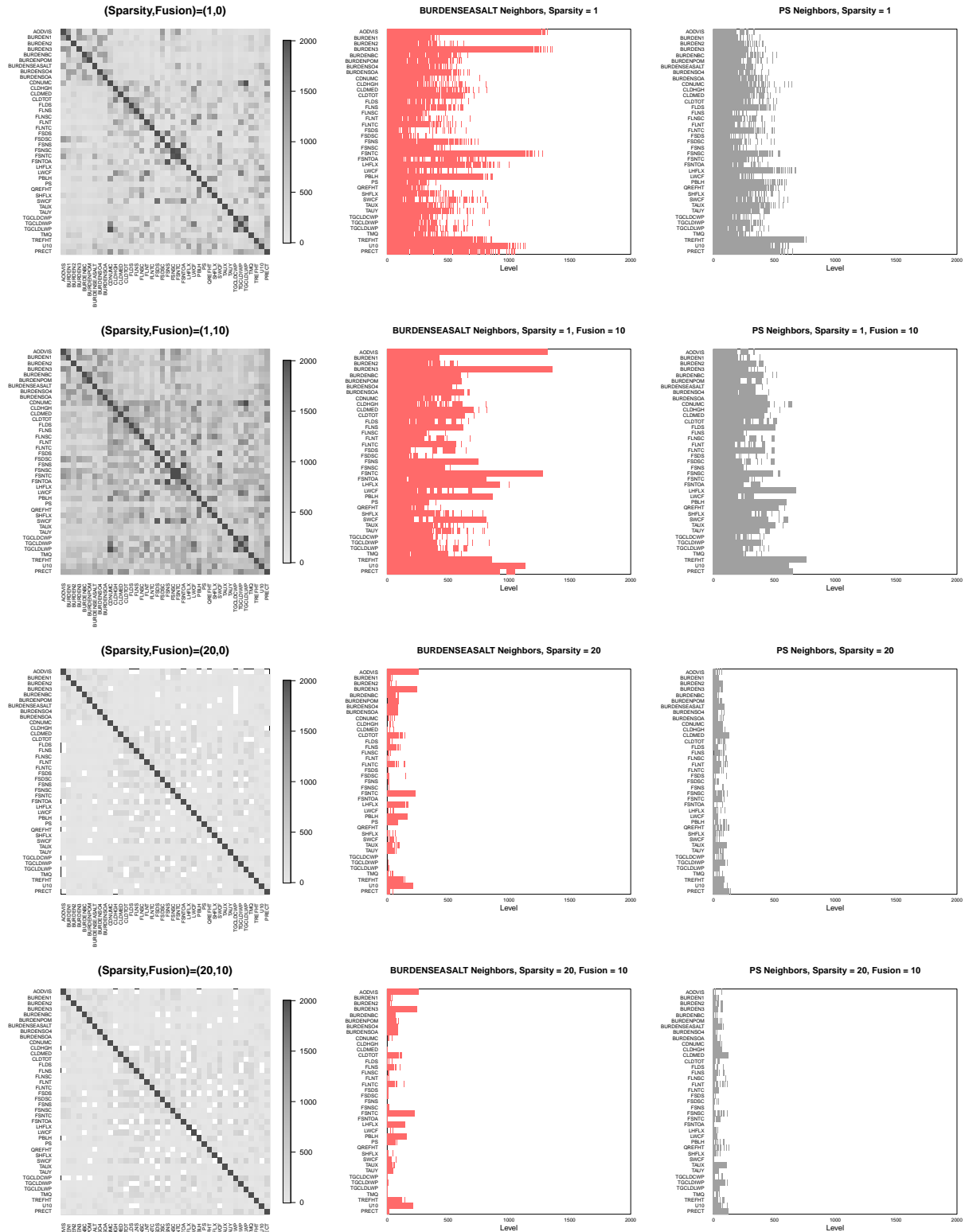


Figure 8: Illustrating how graphical model neighborhoods behave for various penalty choices. Left column counts the nonzeros of  $\hat{Q}_1, \dots, \hat{Q}_{2000}$  by level. Center and right columns show how the neighbors of BURDENSEASALT and PS change over level.



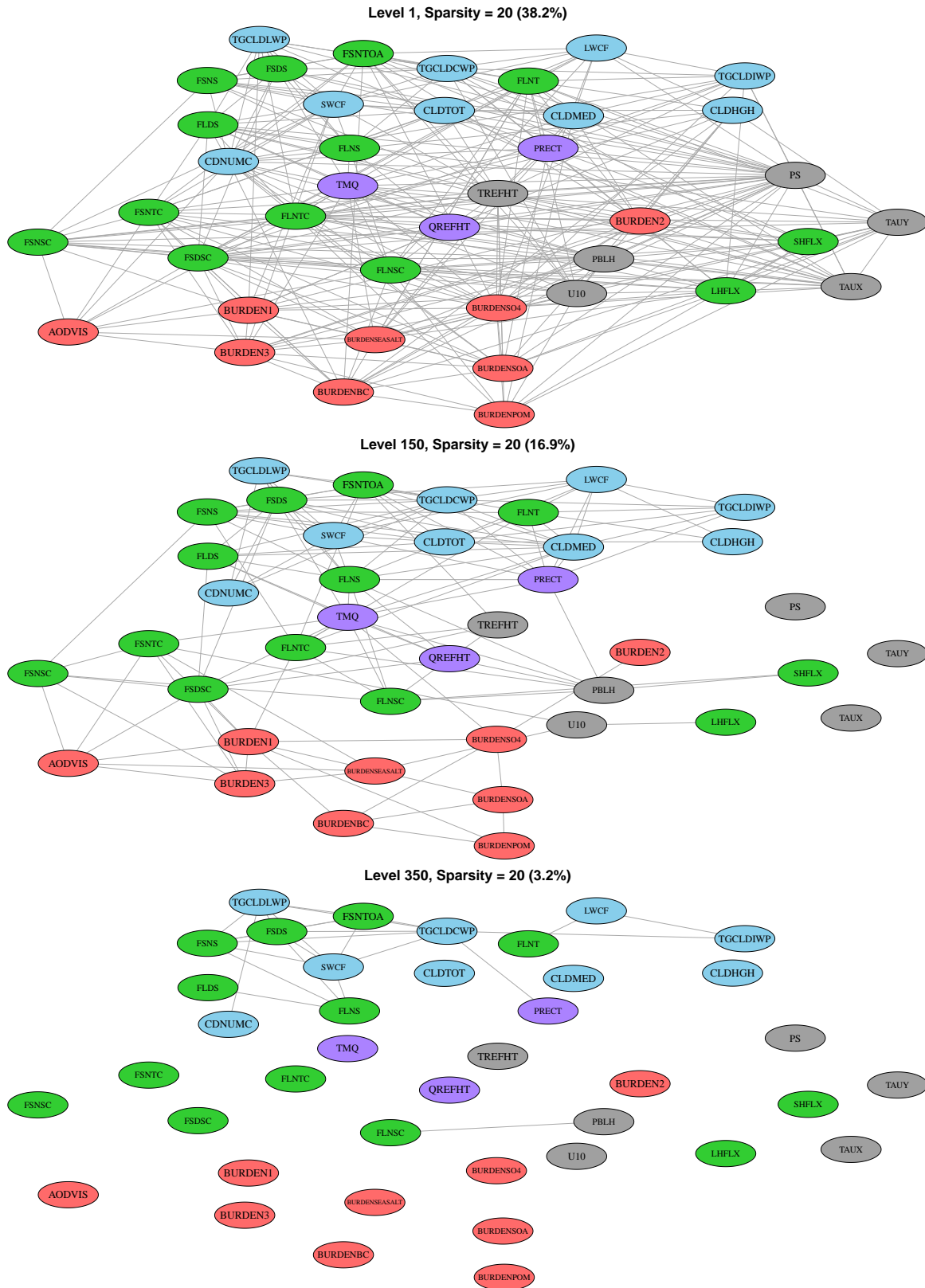


Figure 9: Example estimated graphical models for  $\lambda = 20$ . Low level graphs are noisy, with the Level 1 graph containing 38.2% of all possible connections. Higher level graphs show reasonable variable clusters until eventually no graph edges exist.

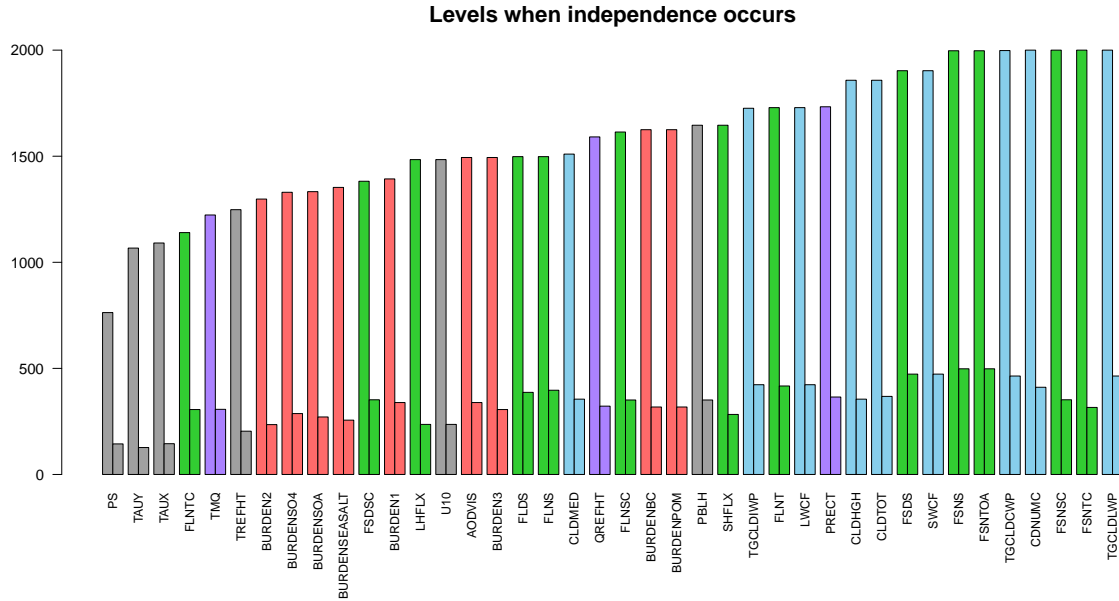


Figure 10: The first level at which a variable becomes (and remains) independent. Variables are ordered in increasing fashion according to the implied independence level for  $\lambda = 1$ . Results for  $\lambda = 20$  accompany the taller bars and show a similar story for variable groups but with earlier levels of independence.

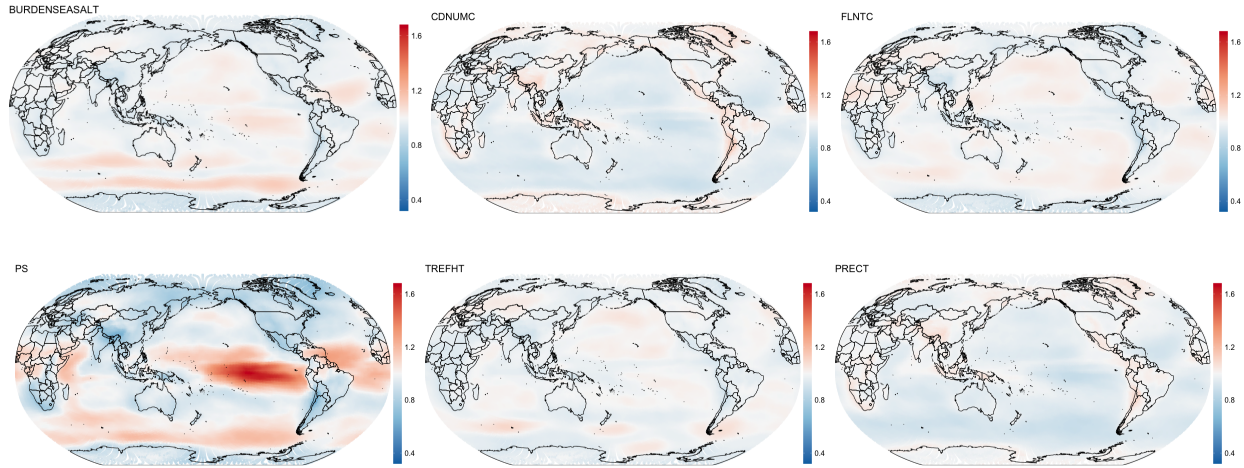


Figure 11: Estimated local standard deviations for six variables. Standardization of the variables is reflected in the color scale, where unit values are colored white. Values above one suggest the empirical standardization does not explain enough variability.

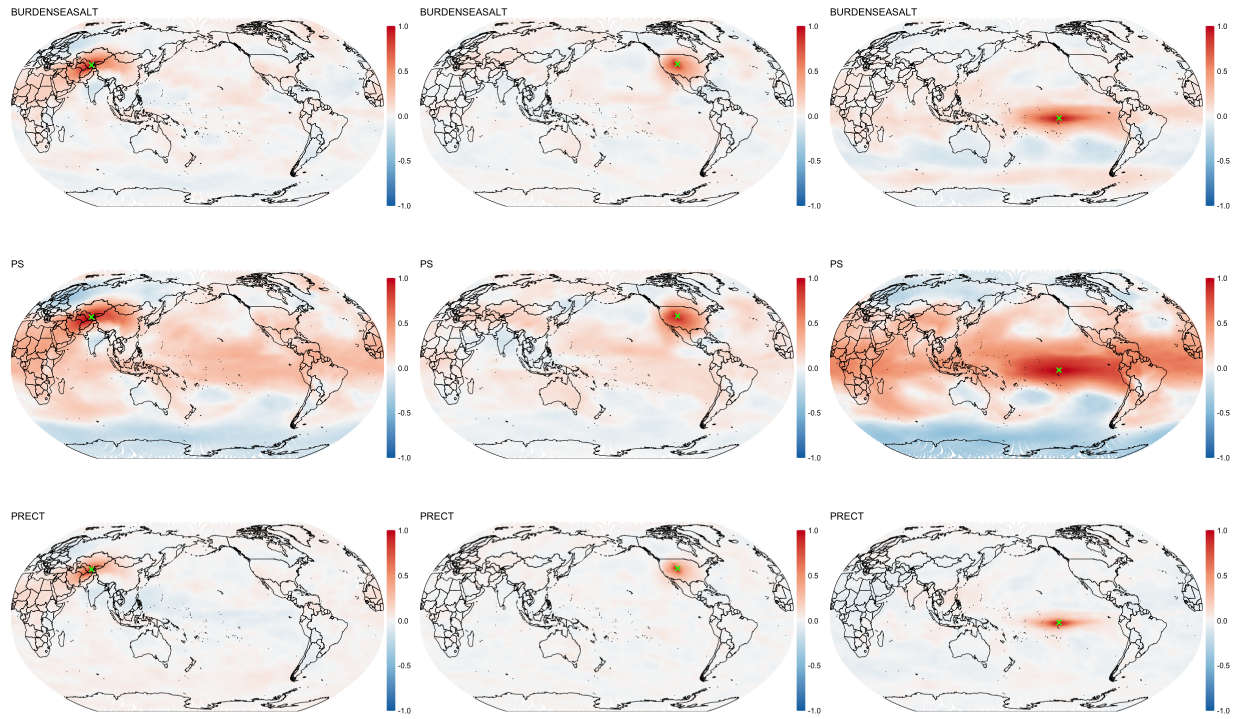


Figure 12: Estimated spatial correlation functions for BURDENSEASALT (top row), PS (middle row), and PRECT (bottom row). Correlation function is centered over Tajikstan in the left column, U.S. in the middle column, and the Pacific Ocean in the right column.

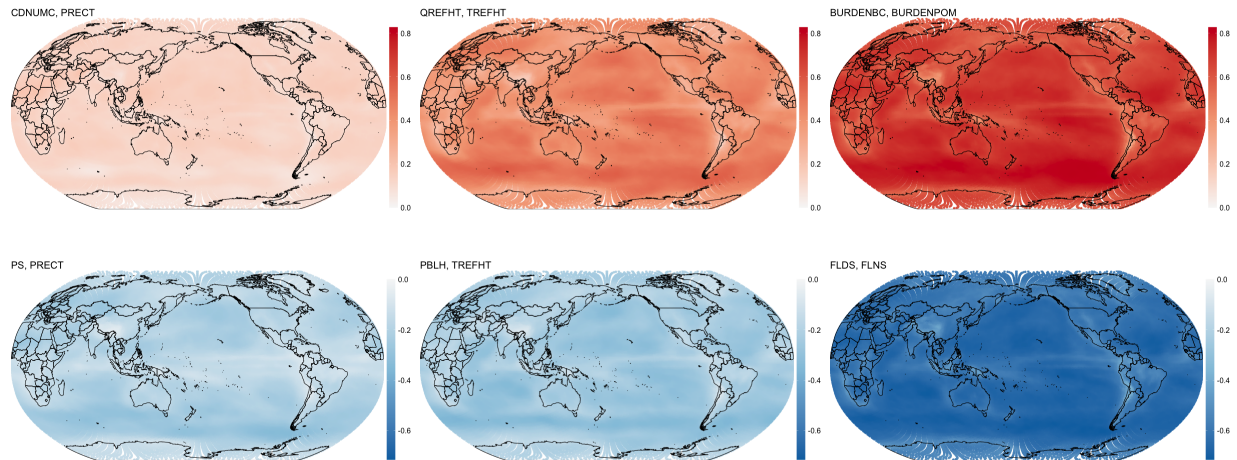


Figure 13: Estimated local cross-correlations for several pairs of variables. Color scale changes between rows to permit easier comparisons between positively correlated variables (top row) and between negatively correlated variables (bottom row).

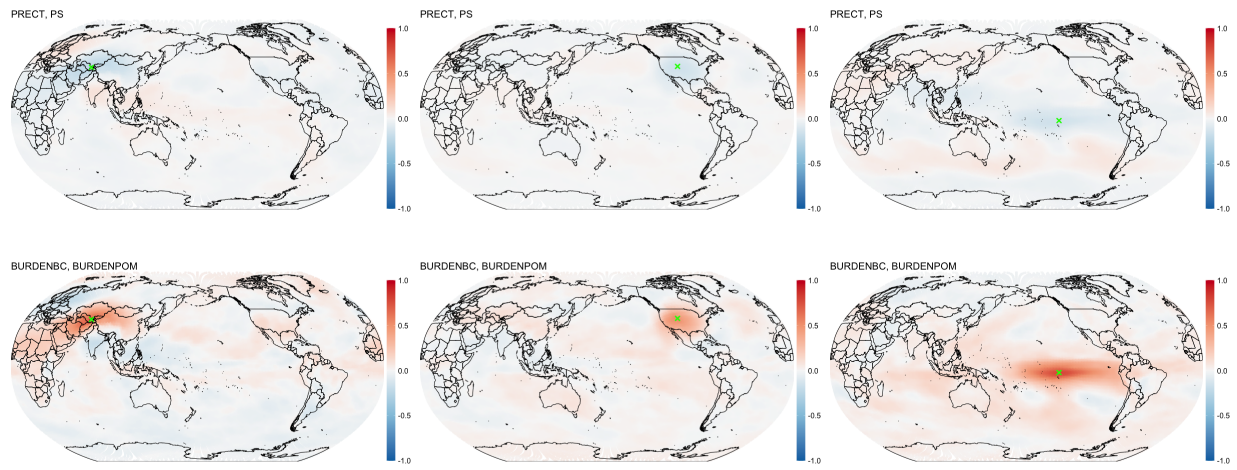


Figure 14: Estimated spatial cross-correlation functions, again centered over Tajikstan in the left column, U.S. in the middle column, and the Pacific Ocean in the right column. Top row shows PRECT and PS which exhibit negative local cross-correlations, while bottom row shows BURDENBC and BURDENPOM which exhibit positive local cross-correlations.

## 5 Conclusion

We have presented a multivariate Gaussian process model which will be applicable in a variety of future endeavors. There are many benefits under this framework: covariance and cross-covariance functions are nonstationary, all likelihood calculations are exact, and computations and storage are cheap when  $\mathbf{W}_1, \dots, \mathbf{W}_L$  are independent and basis functions are orthogonal.

Future experiments could relax the assumption of independent weights and estimate the entire sparse  $pL \times pL$  precision matrix  $\mathbf{Q}$  as in Section 2.1 with the DC algorithm (8). Even if the basis functions are not orthogonal,  $\Phi^T \mathbf{D}^{-1} \Phi = \Phi^T \Phi \otimes \text{diag}(\tau_1^{-2}, \dots, \tau_p^{-2})$  is sparse due to the Kronecker product with a diagonal matrix. In this formulation, it is crucial to rewrite (9) and calculate this linearization term by solving linear systems with the sparse matrix  $\mathbf{Q} + \Phi^T \mathbf{D}^{-1} \Phi$  or its sparse Cholesky decomposition. Note that the dense  $pL \times pL$  linearization matrix must then be stored in memory, and advanced graphical lasso algorithms (Fattahi et al., 2019) must be explored for the subsequent graph estimation. Modeling dependence across basis functions would allow for more flexibility in the cross-covariances, since, with the independence assumption,  $\text{Cov}(Z_i(\mathbf{s}), Z_j(\mathbf{s}')) = \sum_{\ell=1}^L \phi_\ell(\mathbf{s}) ((\mathbf{Q}_\ell)^{-1})_{ij} \phi_\ell(\mathbf{s}') = \text{Cov}(Z_i(\mathbf{s}'), Z_j(\mathbf{s}))$  is symmetric.

We demonstrated that our model can easily fit a large climate ensemble and produce reasonable and interpretable results. Our method also easily scales to computer experiments with high-dimensional inputs (e.g.,  $\mathbf{s} \in \mathbb{R}^d$  with  $d \gg 0$ ). Extending these multivariate basis graphical lasso ideas to a space-time setting could further prove to be fruitful.

## Acknowledgements

This research was supported by NSF. Code is available upon request.



## References

- Apanasovich, T. and Genton, M. G. (2010), “Cross-covariance functions for multivariate random fields based on latent dimensions,” *Biometrika*, 97, 15–30, ISSN 0006-3444, URL <https://doi.org/10.1093/biomet/asp078>.
- Apanasovich, T. V., Genton, M. G., and Sun, Y. (2012), “A valid Matérn class of cross-covariance functions for multivariate random fields with any number of components,” *J. Amer. Statist. Assoc.*, 107, 180–193, ISSN 0162-1459, URL <https://doi.org/10.1080/01621459.2011.643197>.
- Baker, A. H., Hammerling, D. M., Levy, M. N., Xu, H., Dennis, J. M., Eaton, B. E., Edwards, J., Hannay, C., Mickelson, S. A., Neale, R. B., Nychka, D., Shollenberger, J., Tribbia, J., Vertenstein, M., and Williamson, D. (2015), “A new ensemble-based consistency test for the community earth system model (pycect v1.0),” *Geoscientific Model Development*, 8, 2829–2840, URL <https://gmd.copernicus.org/articles/8/2829/2015/>.
- Bruinsma, W., Perin, E., Tebbutt, W., S., H. J., Solin, A., and Turner, R. (2020), “Scalable exact inference in multi-output gaussian processes,” *arXiv: Machine Learning*.
- Calder, C. A. (2007), “Dynamic factor process convolution models for multivariate space-time data with application to air quality assessment,” *Environ. Ecol. Stat.*, 14, 229–247, ISSN 1352-8505, URL <https://doi.org/10.1007/s10651-007-0019-y>.
- Danaher, P., Wang, P., and Witten, D. M. (2014), “The joint graphical lasso for inverse covariance estimation across multiple classes,” *J. R. Stat. Soc. Ser. B. Stat. Methodol.*, 76, 373–397, ISSN 1369-7412, URL <https://doi.org/10.1111/rssb.12033>.
- Datta, A., Banerjee, S., Finley, A. O., and Gelfand, A. E. (2016), “Hierarchical nearest-neighbor gaussian process models for large geostatistical datasets,” *Journal of the American Statistical Association*, 111, 800–812, URL <https://doi.org/10.1080/01621459.2015.1044091>.
- Dey, D., Datta, A., and Banerjee, S. (2020), “Graphical gaussian process models for highly multivariate spatial data,” *arXiv: Statistics*.

- Fattahi, S., Zhang, R. Y., and Sojoudi, S. (2019), “Linear-time algorithm for learning large-scale sparse graphical models,” *IEEE Access*, pp. 1–1, ISSN 2169-3536.
- Friedman, J., Hastie, T., and Tibshirani, R. (2008), “Sparse inverse covariance estimation with the graphical lasso,” *Biostatistics*, 9, 432–441, ISSN 1465-4644, URL <https://www.ncbi.nlm.nih.gov/pmc/articles/PMC3019769/>.
- Furrer, R. and Genton, M. G. (2011), “Aggregation-cokriging for highly multivariate spatial data,” *Biometrika*, 98, 615–631, ISSN 0006-3444, URL <https://doi.org/10.1093/biomet/asr029>.
- Gaspari, G. and Cohn, S. E. (1999), “Construction of correlation functions in two and three dimensions,” *Quarterly Journal of the Royal Meteorological Society*, 125, 723–757, URL <https://rmets.onlinelibrary.wiley.com/doi/abs/10.1002/qj.49712555417>.
- Gelfand, A. E., Schmidt, A. M., Banerjee, S., and Sirmans, C. F. (2004), “Nonstationary multivariate process modeling through spatially varying coregionalization,” *Test*, 13, 263–312, ISSN 1133-0686, URL <https://doi.org/10.1007/BF02595775>, with discussion by Montserrat Fuentes, Dave Higdon and Bruno Sansó and a rejoinder by the authors.
- Genton, M. G. and Kleiber, W. (2015), “Cross-covariance functions for multivariate geostatistics,” *Statist. Sci.*, 30, 147–163, ISSN 0883-4237, URL <https://doi.org/10.1214/14-STS487>.
- Gneiting, T., Kleiber, W., and Schlather, M. (2010), “Matérn cross-covariance functions for multivariate random fields,” *J. Amer. Statist. Assoc.*, 105, 1167–1177, ISSN 0162-1459, URL <https://doi.org/10.1198/jasa.2010.tm09420>.
- Goulard, M. and Voltz, M. (1992), “Linear coregionalization model: Tools for estimation and choice of cross-variogram matrix,” *Mathematical Geology*, 24, 269–286.
- Guinness, J. (2018), “Nonparametric spectral methods for multivariate spatial and spatial-temporal data,” *arXiv: Statistics*.
- Harville, D. A. (1997), *Matrix algebra from a statistician’s perspective*, Springer-Verlag, New York, ISBN 0-387-94978-X, URL <https://doi.org/10.1007/b98818>.

- Hsieh, C.-J., Dhillon, I. S., Ravikumar, P. K., Becker, S., and Olsen, P. A. (2014a), “Quic & dirty: A quadratic approximation approach for dirty statistical models,” in *Advances in Neural Information Processing Systems 27*, eds. Z. Ghahramani, M. Welling, C. Cortes, N. D. Lawrence, and K. Q. Weinberger, Curran Associates, Inc., pp. 2006–2014, URL <http://papers.nips.cc/paper/5578-quic-dirty-a-quadratic-approximation-approach-for-dirty-statistical-models.pdf>.
- Hsieh, C.-J., Sustik, M. A., Dhillon, I. S., and Ravikumar, P. (2014b), “QUIC: quadratic approximation for sparse inverse covariance estimation,” *J. Mach. Learn. Res.*, 15, 2911–2947, ISSN 1532-4435.
- Ippoliti, L., Valentini, P., and Gamerman, D. (2012), “Space-time modelling of coupled spatiotemporal environmental variables,” *J. R. Stat. Soc. Ser. C. Appl. Stat.*, 61, 175–200, ISSN 0035-9254, URL <https://doi.org/10.1111/j.1467-9876.2011.01011.x>.
- Kleiber, W. (2017), “Coherence for multivariate random fields,” *Statist. Sinica*, 27, 1675–1697, ISSN 1017-0405.
- Kleiber, W. and Genton, M. G. (2013), “Spatially varying cross-correlation coefficients in the presence of nugget effects,” *Biometrika*, 100, 213–220.
- Kleiber, W. and Nychka, D. (2012), “Nonstationary modeling for multivariate spatial processes,” *J. Multivariate Anal.*, 112, 76–91, ISSN 0047-259X, URL <https://doi.org/10.1016/j.jmva.2012.05.011>.
- Kleiber, W., Nychka, D., and Bandyopadhyay, S. (2019), “A model for large multivariate spatial data sets,” *Statist. Sinica*, 29, 1085–1104, ISSN 1017-0405.
- Kleiber, W. and Porcu, E. (2014), “Nonstationary matrix covariances: compact support, long range dependence and quasi-arithmetic constructions,” *Stochastic Environmental Research and Risk Assessment*, 29, 193–204.
- Krock, M., Kleiber, W., and Becker, S. (2020), “Nonstationary modeling with sparsity for



- spatial data via the basis graphical lasso,” *Journal of Computational and Graphical Statistics*, 0, 1–36, URL <https://doi.org/10.1080/10618600.2020.1811103>.
- Le, N. D. and Zidek, J. V. (2006), *Statistical analysis of environmental space-time processes*, Springer Series in Statistics, Springer, New York, ISBN 0-387-26209-1; 978-0387-26209-3.
- Majumdar, A. and Gelfand, A. E. (2007), “Multivariate spatial modeling for geostatistical data using convolved covariance functions,” *Math. Geol.*, 39, 225–245, ISSN 0882-8121, URL <https://doi.org/10.1007/s11004-006-9072-6>.
- Majumdar, A., Paul, D., and Bautista, D. (2010), “A generalized convolution model for multivariate nonstationary spatial processes,” *Statist. Sinica*, 20, 675–695, ISSN 1017-0405.
- Nychka, D., Bandyopadhyay, S., Hammerling, D., Lindgren, F., and Sain, S. (2015), “A multiresolution Gaussian process model for the analysis of large spatial datasets,” *J. Comput. Graph. Statist.*, 24, 579–599, ISSN 1061-8600, URL <https://doi.org/10.1080/10618600.2014.914946>.
- Pollice, A. and Jona Lasinio, G. (2010), “A multivariate approach to the analysis of air quality in a high environmental risk area,” *Environmetrics*, 21, 741–754, ISSN 1180-4009, URL <https://doi.org/10.1002/env.1059>.
- Rue, H. and Held, L. (2005), *Gaussian Markov Random Fields: Theory And Applications (Monographs on Statistics and Applied Probability)*, Chapman & Hall/CRC, ISBN 1584884320.
- Schmidt, A. M. and Gelfand, A. E. (2003), “A bayesian coregionalization approach for multivariate pollutant data,” *Journal of Geophysical Research: Atmospheres*, 108, URL <https://agupubs.onlinelibrary.wiley.com/doi/abs/10.1029/2002JD002905>.
- Shaddick, G. and Wakefield, J. (2002), “Modelling daily multivariate pollutant data at multiple sites,” *J. Roy. Statist. Soc. Ser. C*, 51, 351–372, ISSN 0035-9254, URL <https://doi.org/10.1111/1467-9876.00273>.

- Stein, M. L. (1999), *Interpolation of Spatial Data: Some Theory for Kriging*, New York: Springer-Verlag.
- Stein, M. L. (2014), “Limitations on low rank approximations for covariance matrices of spatial data,” *Spat. Stat.*, 8, 1–19, URL <https://doi.org/10.1016/j.spasta.2013.06.003>.
- Taylor-Rodriguez, D., Finley, A., Datta, A., Babcock, C., Andersen, H., Cook, B., Morton, D., and Banerjee, S. (2019), “Spatial factor models for high-dimensional and large spatial data: An application in forest variable mapping,” *Statistica Sinica*, 29, 1155–1180, ISSN 1017-0405.
- Teh, Y., Seeger, M. W., and Jordan, M. I. (2005), “Semiparametric latent factor models,” in *AISTATS*.
- Titsias, M. (2009), “Variational learning of inducing variables in sparse gaussian processes,” in *Proceedings of the Twelfth International Conference on Artificial Intelligence and Statistics*, eds. D. van Dyk and M. Welling, Hilton Clearwater Beach Resort, Clearwater Beach, Florida USA: PMLR, volume 5 of *Proceedings of Machine Learning Research*, pp. 567–574, URL <http://proceedings.mlr.press/v5/titsias09a.html>.
- Ver Hoef, J. M. and Barry, R. P. (1998), “Constructing and fitting models for cokriging and multivariable spatial prediction,” *J. Statist. Plann. Inference*, 69, 275–294, ISSN 0378-3758, URL [https://doi.org/10.1016/S0378-3758\(97\)00162-6](https://doi.org/10.1016/S0378-3758(97)00162-6).
- Wackernagel, H. (2003), *Multivariate Geostatistics: An Introduction with Applications*, Springer Berlin Heidelberg, ISBN 9783540441427, URL <https://books.google.com/books?id=Rhr7bgLWxx4C>.
- Wikle, C. K. (2010), “Low rank representations for spatial processes,” in *Handbook of Spatial Statistics*, eds. A. E. Gelfand, P. Diggle, P. Guttorp, and M. Fuentes, Boca Raton: Chapman & Hall / CRC, pp. 107–118.
- Yang, S., Lu, Z., Shen, X., Wonka, P., and Ye, J. (2015), “Fused multiple graphical

lasso,” *SIAM J. Optim.*, 25, 916–943, ISSN 1052-6234, URL <https://doi.org/10.1137/130936397>.

## 6 Appendix

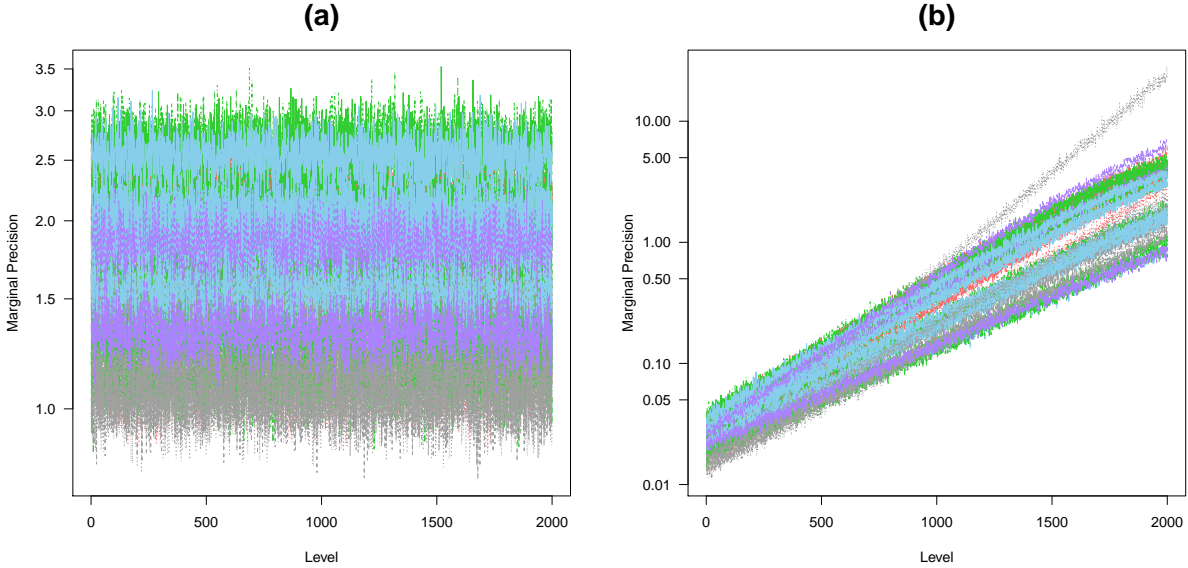


Figure 15: (a) Marginal precision estimates for the simulated white noise data. In this case, values should be constant across level. (b) Marginal precision estimates for the simulated correlated data. Corresponds to the parameterization with exponentially growing precision matrices. Note the logarithmic scale on the  $y$ -axis, so the exponential growth is captured well. The noticeable grey line in (b) is the pressure variable.



	$\tau$	exponential	$\psi$	$\eta$	constant	$\eta$
AODVIS	0.1285	0.0029	0.1046	1.91	0.2049	2.89
BURDEN1	0.1059	0.0030	0.1047	2.66	0.2043	4.27
BURDEN2	0.1490	0.0027	0.1094	1.36	0.2055	2.13
BURDEN3	0.1318	0.0029	0.1065	1.77	0.2049	2.74
BURDENBC	0.1217	0.0029	0.1067	2.05	0.2047	3.22
BURDENPOM	0.1283	0.0028	0.1070	1.86	0.2049	2.89
BURDENSEASALT	0.1404	0.0028	0.1076	1.55	0.2052	2.41
BURDENSO4	0.1327	0.0028	0.1063	1.76	0.2050	2.70
BURDENSOA	0.1265	0.0029	0.1072	1.86	0.2048	2.98
CDNUMC	0.2301	0.0020	0.1116	0.75	0.2088	0.87
CLDHGH	0.1947	0.0024	0.1072	0.94	0.2071	1.23
CLDMED	0.2238	0.0023	0.1109	0.70	0.2085	0.92
CLDTOT	0.2122	0.0024	0.1096	0.76	0.2079	1.03
FLDS	0.1558	0.0028	0.1065	1.28	0.2057	1.95
FLNS	0.1524	0.0029	0.1042	1.34	0.2056	2.04
FLNSC	0.1435	0.0028	0.1059	1.55	0.2053	2.31
FLNT	0.1257	0.0029	0.1037	2.04	0.2048	3.02
FLNTC	0.1293	0.0030	0.1073	1.75	0.2049	2.85
FSDS	0.1315	0.0028	0.1014	2.03	0.2049	2.75
FSDSC	0.1327	0.0029	0.1059	1.74	0.2050	2.70
FSNS	0.1363	0.0026	0.1030	1.94	0.2051	2.56
FSNSC	0.1761	0.0024	0.1087	1.12	0.2064	1.51
FSNTC	0.1947	0.0023	0.1114	0.91	0.2071	1.23
FSNTOA	0.1520	0.0025	0.1040	1.58	0.2055	2.05
LHFLX	0.2390	0.0021	0.1143	0.63	0.2092	0.80
LWCF	0.1563	0.0026	0.1033	1.46	0.2057	1.94
PBLH	0.2223	0.0022	0.1101	0.74	0.2084	0.93
PS	0.0625	0.0038	0.1138	5.22	0.2035	12.36
QREFHT	0.1387	0.0028	0.1066	1.60	0.2051	2.47
SHFLX	0.2286	0.0021	0.1126	0.70	0.2087	0.88
SWCF	0.1505	0.0026	0.1026	1.58	0.2055	2.09
TAUX	0.1835	0.0025	0.1092	0.99	0.2067	1.39
TAUY	0.1972	0.0023	0.1087	0.92	0.2072	1.20
TGCLDCWP	0.1730	0.0026	0.1045	1.17	0.2063	1.57
TGCLDIWP	0.2050	0.0023	0.1083	0.88	0.2076	1.11
TGCLDLWP	0.2014	0.0022	0.1088	0.93	0.2074	1.15
TMQ	0.1067	0.0031	0.1064	2.47	0.2043	4.21
TREFHT	0.1701	0.0026	0.1097	1.09	0.2062	1.63
U10	0.2124	0.0022	0.1106	0.80	0.2079	1.03
PRECT	0.2491	0.0020	0.1150	0.61	0.2098	0.73

Table 2: Estimates of standard deviation  $\tau$  with  $L = 2000$  EOFs, obtained independently for each variable. For the exponential case,  $Q$  is diagonal with  $\ell^{\text{th}}$  element  $\psi^2 e^{\alpha \ell}$ . For the constant case,  $Q$  has constant diagonal  $\psi^2$ . Also,  $\eta$  is the signal-to-noise ratio on  $10^6$  scale.